

21 cm observation of LSS at $z \sim 1$

Instrument sensitivity and foreground subtraction

R. Ansari^{1,2}, J.E. Campagne³, P.Colom⁵, J.M. Le Goff⁴, C. Magneville⁴, J.M. Martin⁵, M. Moniez³, J.Rich⁴, and C.Yèche⁴

¹ Université Paris-Sud, LAL, UMR 8607, F-91898 Orsay Cedex, France

² CNRS/IN2P3, F-91405 Orsay, France

e-mail: ansari@lal.in2p3.fr

³ Laboratoire de l'Accélérateur Linéaire, CNRS-IN2P3, Université Paris-Sud, B.P. 34, 91898 Orsay Cedex, France

⁴ CEA, DSM/IRFU, Centre d'Etudes de Saclay, F-91191 Gif-sur-Yvette, France

⁵ GEPI, UMR 8111, Observatoire de Paris, 61 Ave de l'Observatoire, 75014 Paris, France

Received July 15, 2011; accepted xxxx, 2011

ABSTRACT

Context. Large Scale Structures (LSS) in the universe can be traced using the neutral atomic hydrogen H_I through its 21 cm emission. Such a 3D matter distribution map can be used to test the Cosmological model and to constrain the Dark Energy properties or its equation of state. A novel approach, called intensity mapping can be used to map the H_I distribution, using radio interferometers with large instantaneous field of view and waveband.

Aims. In this paper, we study the sensitivity of different radio interferometer configurations, or multi-beam instruments for the observation of large scale structures and BAO oscillations in 21 cm and we discuss the problem of foreground removal.

Methods. For each configuration, we determine instrument response by computing the (u,v) or Fourier angular frequency plane coverage using visibilities. The (u,v) plane response is the noise power spectrum, hence the instrument sensitivity for LSS $P(k)$ measurement. We describe also a simple foreground subtraction method to separate LSS 21 cm signal from the foreground due to the galactic synchrotron and radio sources emission.

Results. We have computed the noise power spectrum for different instrument configuration as well as the extracted LSS power spectrum, after separation of 21cm-LSS signal from the foregrounds. We have also obtained the uncertainties on the Dark Energy parameters for an optimized 21 cm BAO survey.

Conclusions. We show that a radio instrument with few hundred simultaneous beams and a collecting area of $\sim 10000\text{m}^2$ will be able to detect BAO signal at redshift $z \sim 1$ and will be competitive with optical surveys.

Key words. large-scale structure of Universe – dark energy – Instrumentation: interferometers – Radio lines; galaxies – Radio continuum: general

1. Introduction

The study of the statistical properties of Large Scale Structure (LSS) in the Universe and their evolution with redshift is one the major tools in observational cosmology. These structures are usually mapped through optical observation of galaxies which are used as a tracer of the underlying matter distribution. An alternative and elegant approach for mapping the matter distribution, using neutral atomic hydrogen (H_I) as a tracer with intensity mapping, has been proposed in recent years (Peterson et al. (2006)) (Chang et al. (2008)). Mapping the matter distribution using H_I 21 cm emission as a tracer has been extensively discussed in literature (Furlanetto et al. (2006)) (Tegmark & Zaldarriaga (2009)) and is being used in projects such as LOFAR (Rotter et al. (2006)) or MWA (Bowman et al. (2009)) to observe reionisation at redshifts $z \sim 10$.

Evidence in favor of the acceleration of the expansion of the universe have been accumulated over the last twelve years, thanks to the observation of distant supernovae, CMB anisotropies and detailed analysis of the LSS. A cosmological Constant (Λ) or new cosmological energy density called *Dark Energy* has been advocated as the origin of this acceleration.

Dark Energy is considered as one of the most intriguing puzzles in Physics and Cosmology. Several cosmological probes can be used to constrain the properties of this new cosmic fluid, more precisely its equation of state: The Hubble Diagram, or luminosity distance as a function of redshift of supernovae as standard candles, galaxy clusters, weak shear observations and Baryon Acoustic Oscillations (BAO).

BAO are features imprinted in the distribution of galaxies, due to the frozen sound waves which were present in the photon-baryon plasma prior to recombination at $z \sim 1100$. This scale can be considered as a standard ruler with a comoving length of $\sim 150\text{Mpc}$. These features have been first observed in the CMB anisotropies and are usually referred to as *acoustic peaks* (Mauskopf et al. (2000), Larson et al. (2011)). The BAO modulation has been subsequently observed in the distribution of galaxies at low redshift ($z < 1$) in the galaxy-galaxy correlation function by the SDSS (Eisenstein et al. (2005)) (Percival et al. (2007)) (Percival et al. (2010)), 2dGFRS (Cole et al. (2005)) as well as WiggleZ (Blake et al. (2011)) optical galaxy surveys.

Ongoing (Eisenstein et al. (2011)) or future surveys (LSST.Science) plan to measure precisely the BAO

scale in the redshift range $0 \lesssim z \lesssim 3$, using either optical observation of galaxies or through 3D mapping Lyman α absorption lines toward distant quasars (McDonald et al. (2006)), (McDonald & Eisenstein (2007)). Radio observation of the 21 cm emission of neutral hydrogen appears as a very promising technique to map matter distribution up to redshift $z \sim 3$, complementary to optical surveys, especially in the optical redshift desert range $1 \lesssim z \lesssim 2$, and possibly up to the reionization redshift (Wyithe et al. (2008)).

In section 2, we discuss the intensity mapping and its potential for measurement of the H_I mass distribution power spectrum. The method used in this paper to characterize a radio instrument response and sensitivity for $P_{H_I}(k)$ is presented in section 3. We show also the results for the 3D noise power spectrum for several instrument configurations. The contribution of foreground emissions due to the galactic synchrotron and radio sources is described in section 4, as well as a simple component separation method. The performance of this method using two different sky models is also presented in section 4. The constraints which can be obtained on the Dark Energy parameters and DETF figure of merit for typical 21 cm intensity mapping survey are discussed in section 5.

2. Intensity mapping and H_I power spectrum

2.1. 21 cm intensity mapping

Most of the cosmological information in the LSS is located at large scales ($\gtrsim 1$ deg), while the interpretation at smallest scales might suffer from the uncertainties on the non linear clustering effects. The BAO features in particular are at the degree angular scale on the sky and thus can be resolved easily with a rather modest size radio instrument (diameter $D \lesssim 100$ m). The specific BAO clustering scale (k_{BAO}) can be measured both in the transverse plane (angular correlation function, (k_{BAO}^\perp)) or along the longitudinal (line of sight or redshift (k_{BAO}^\parallel)) direction. A direct measurement of the Hubble parameter $H(z)$ can be obtained by comparing the longitudinal and transverse BAO scales. A reasonably good redshift resolution $\delta z \lesssim 0.01$ is needed to resolve longitudinal BAO clustering, which is a challenge for photometric optical surveys.

In order to obtain a measurement of the LSS power spectrum with small enough statistical uncertainties (sample or cosmic variance), a large volume of the universe should be observed, typically few Gpc^3 . Moreover, stringent constraint on DE parameters can only be obtained when comparing the distance or Hubble parameter measurements with DE models as a function of redshift, which requires a significant survey depth $\Delta z \gtrsim 1$.

Radio instruments intended for BAO surveys must thus have large instantaneous field of view (FOV $\gtrsim 10$ deg²) and large bandwidth ($\Delta\nu \gtrsim 100$ MHz) to explore large redshift domains.

Although the application of 21 cm radio survey to cosmology, in particular LSS mapping has been discussed in length in the framework of large future instruments, such as the SKA (e.g SKA.Science, Abdalla & Rawlings (2005)), the method envisaged has been mostly through the detection of galaxies as H_I compact sources. However, extremely large radio telescopes are required to detect H_I sources at cosmological distances. The sensitivity (or detection threshold) limit S_{lim} for the total power from the two polarisations of a radio instrument characterized by an effective collecting area A , and system temperature T_{sys} can be written as

$$S_{lim} = \frac{\sqrt{2} k_B T_{sys}}{A \sqrt{t_{int} \delta\nu}} \quad (1)$$

$A(m^2)$	$T_{sys}(K)$	$S_{lim}(\mu Jy)$	z	$d_L(Mpc)$	$S_{21}(\mu Jy)$
5000	50	66	0.25	1235	175
5000	25	33	0.50	2800	40
100 000	50	3.3	1.0	6600	9.6
100 000	25	1.66	1.5	10980	3.5
500 000	50	0.66	2.0	15710	2.5
500 000	25	0.33	2.5	20690	1.7

Table 1. Sensitivity or source detection limit for 1 day integration time (86400 s) and 1 MHz frequency band (left). Source 21 cm brightness for $10^{10} M_\odot H_I$ for different redshifts (right)

where t_{int} is the total integration time and $\delta\nu$ is the detection frequency band. In table 1 (left) we have computed the sensitivity for 6 different sets of instrument effective area and system temperature, with a total integration time of 86400 seconds (1 day) over a frequency band of 1 MHz. The width of this frequency band is well adapted to detection of H_I source with an intrinsic velocity dispersion of few 100 km/s. These detection limits should be compared with the expected 21 cm brightness S_{21} of compact sources which can be computed using the expression below (e.g. Binney & Merrifield (1998)) :

$$S_{21} \simeq 0.021 \mu Jy \frac{M_{H_I}}{M_\odot} \times \left(\frac{1 \text{ Mpc}}{d_L(z)} \right)^2 \times \frac{200 \text{ km/s}}{\sigma_v} (1+z) \quad (2)$$

where M_{H_I} is the neutral hydrogen mass, $d_L(z)$ is the luminosity distance and σ_v is the source velocity dispersion.

In table 1 (right), we show the 21 cm brightness for compact objects with a total H_I mass of $10^{10} M_\odot$ and an intrinsic velocity dispersion of 200 km/s. The luminosity distance is computed for the standard Λ CDM universe. $10^9 - 10^{10} M_\odot$ of neutral gas mass is typical for large galaxies (Lah et al. (2009)). It is clear that detection of H_I sources at cosmological distances would require collecting area in the range of $10^6 m^2$.

Intensity mapping has been suggested as an alternative and economic method to map the 3D distribution of neutral hydrogen by (Chang et al. (2008)) and further studied by (Ansari et al. (2008)) (Seo et al (2010)). In this approach, sky brightness map with angular resolution $\sim 10-30$ arc.min is made for a wide range of frequencies. Each 3D pixel (2 angles Θ , frequency ν or wavelength λ) would correspond to a cell with a volume of $\sim 10^3 Mpc^3$, containing ten to hundred galaxies and a total H_I mass $\sim 10^{12} M_\odot$. If we neglect local velocities relative to the Hubble flow, the observed frequency ν would be translated to the emission redshift z through the well known relation:

$$z(\nu) = \frac{\nu_{21} - \nu}{\nu}; \nu(z) = \frac{\nu_{21}}{(1+z)} \text{ with } \nu_{21} = 1420.4 \text{ MHz} \quad (3)$$

$$z(\lambda) = \frac{\lambda - \lambda_{21}}{\lambda_{21}}; \lambda(z) = \lambda_{21} \times (1+z) \text{ with } \lambda_{21} = 0.211 \text{ m} \quad (4)$$

The large scale distribution of the neutral hydrogen, down to angular scales of ~ 10 arc.min can then be observed without the detection of individual compact H_I sources, using the set of sky brightness map as a function of frequency (3D-brightness map) $B_{21}(\Theta, \lambda)$. The sky brightness B_{21} (radiation power/unit solid angle/unit surface/unit frequency) can be converted to brightness temperature using the well known black body Rayleigh-Jeans approximation:

$$B(T, \lambda) = \frac{2k_B T}{\lambda^2}$$

2.2. H_I power spectrum and BAO

In the absence of any foreground or background radiation, the brightness temperature for a given direction and wavelength $T_{21}(\Theta, \lambda)$ would be proportional to the local H_I number density $n_{H_I}(\Theta, z)$ through the relation:

$$T_{21}(\Theta, \lambda(z)) = \frac{3}{32\pi} \frac{h}{k_B} A_{21} \lambda_{21}^2 \times \frac{c}{H(z)} (1+z)^2 \times n_{H_I}(\Theta, z) \quad (5)$$

where $A_{21} = 2.85 \cdot 10^{-15} \text{s}^{-1}$ (Lang (1999)) is the spontaneous 21 cm emission coefficient, h is the Planck constant, c the speed of light, k_B the Boltzmann constant and $H(z)$ is the Hubble parameter at the emission redshift. For a Λ CDM universe and neglecting radiation energy density, the Hubble parameter can be expressed as:

$$H(z) \simeq h_{100} \left[\Omega_m (1+z)^3 + \Omega_\Lambda \right]^{\frac{1}{2}} \times 100 \text{ km/s/Mpc} \quad (6)$$

Introducing the H_I mass fraction relative to the total baryon mass f_{H_I} , the neutral hydrogen number density relative fluctuations can be written as, and the corresponding 21 cm emission temperature can be written as:

$$n_{H_I}(\Theta, z(\lambda)) = f_{H_I}(z) \times \Omega_B \frac{\rho_{crit}}{m_H} \times \left(\frac{\delta \rho_{H_I}}{\bar{\rho}_{H_I}}(\Theta, z) + 1 \right) \quad (7)$$

$$T_{21}(\Theta, \lambda(z)) = \bar{T}_{21}(z) \times \left(\frac{\delta \rho_{H_I}}{\bar{\rho}_{H_I}}(\Theta, z) + 1 \right) \quad (8)$$

where Ω_B, ρ_{crit} are respectively the present day mean baryon cosmological and critical densities, m_H is the hydrogen atom mass, and $\frac{\delta \rho_{H_I}}{\bar{\rho}_{H_I}}$ is the H_I density fluctuations.

The present day neutral hydrogen fraction $f_{H_I}(0)$ present in local galaxies has been measured to be $\sim 1\%$ of the baryon density (Zwaan et al.(2005)):

$$\Omega_{H_I} \simeq 3.5 \cdot 10^{-4} \sim 0.008 \times \Omega_B$$

The neutral hydrogen fraction is expected to increase with redshift, as gas is used in star formation during galaxy formation and evolution. Study of Lyman- α absorption indicate a factor 3 increase in the neutral hydrogen fraction at $z = 1.5$ in the intergalactic medium (Wolf et al.(2005)), compared to its present day value $f_{H_I}(z = 1.5) \sim 0.025$. The 21 cm brightness temperature and the corresponding power spectrum can be written as (Barkana & Loeb (2007) and Madau et al. (1997)) :

$$P_{T_{21}}(k) = (\bar{T}_{21}(z))^2 P(k) \quad (9)$$

$$\bar{T}_{21}(z) \simeq 0.084 \text{ mK} \frac{(1+z)^2 h_{100}}{\sqrt{\Omega_m(1+z)^3 + \Omega_\Lambda}} \frac{\Omega_B}{0.044} \frac{f_{H_I}(z)}{0.01} \quad (10)$$

The table 2 shows the mean 21 cm brightness temperature for the standard Λ CDM cosmology and either a constant H_I mass fraction $f_{H_I} = 0.01$, or linearly increasing $f_{H_I} \simeq 0.008 \times (1+z)$. Figure 1 shows the 21 cm emission power spectrum at several redshifts, with a constant neutral fraction at 2% ($f_{H_I} = 0.02$). The matter power spectrum has been computed using the Eisenstein & Hu (1998) parametrisation. The correspondence with the angular scales is also shown for the standard WMAP Λ CDM cosmology, according to the relation:

$$\theta_k = \frac{2\pi}{k d_A(z)(1+z)} \quad k = \frac{2\pi}{\theta_k d_A(z)(1+z)} \quad (11)$$

where k is the comoving wave vector and $d_A(z)$ is the angular diameter distance.

z	0.25	0.5	1.	1.5	2.	2.5	3.
(a) \bar{T}_{21}	0.085	0.107	0.145	0.174	0.195	0.216	0.234
(b) \bar{T}_{21}	0.085	0.128	0.232	0.348	0.468	0.605	0.749

Table 2. Mean 21 cm brightness temperature in mK, as a function of redshift, for the standard Λ CDM cosmology with constant H_I mass fraction at $f_{H_I}(z)=0.01$ (a) or linearly increasing mass fraction (b) $f_{H_I}(z) = 0.008(1+z)$

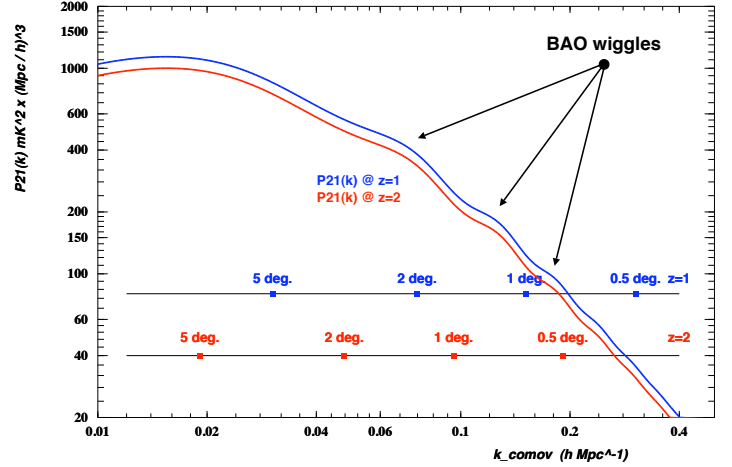


Fig. 1. H_I 21 cm emission power spectrum at redshifts $z=1$ (blue) and $z=2$ (red), with neutral gas fraction $f_{H_I} = 2\%$

3. interferometric observations and $P(k)$ measurement sensitivity

3.1. Instrument response

We introduce briefly here the principles of interferometric observations and the definition of quantities useful for our calculations. Interested reader may refer to (Thompson, Moran & Swenson (2001)) for a detailed and complete presentation of observation methods and signal processing in radio astronomy. In astronomy we are usually interested in measuring the sky emission intensity, $I(\Theta, \lambda)$ in a given wave band, as a function of the sky direction. In radio astronomy and interferometry in particular, receivers are sensitive to the sky emission complex amplitudes. However, for most sources, the phases vary randomly with a spatial correlation length significantly smaller than the instrument resolution.

$$I(\Theta, \lambda) = |A(\Theta, \lambda)|^2, \quad I \in \mathbb{R}, A \in \mathbb{C} \quad (12)$$

$$\langle A(\Theta, \lambda) A^*(\Theta', \lambda) \rangle_{time} = 0 \quad \text{for } \Theta \neq \Theta' \quad (13)$$

A single receiver can be characterized by its angular complex amplitude response $B(\Theta, \nu)$ and its position \mathbf{r} in a reference frame. the waveform complex amplitude s measured by the receiver, for each frequency can be written as a function of the electromagnetic wave vector $\mathbf{k}_{EM}(\Theta, \lambda)$:

$$s(\lambda) = \int d\Theta A(\Theta, \lambda) B(\Theta, \lambda) e^{i(\mathbf{k}_{EM} \cdot \mathbf{r})} \quad (14)$$

We have set the electromagnetic (EM) phase origin at the center of the coordinate frame and the EM wave vector is related to the wavelength λ through the usual equation $|\mathbf{k}_{EM}| = 2\pi/\lambda$. The receiver beam or antenna lobe $L(\Theta, \lambda)$ corresponds to the receiver intensity response:

$$L(\Theta, \lambda) = B(\Theta, \lambda) B^*(\Theta, \lambda) \quad (15)$$

The visibility signal of two receivers corresponds to the time averaged correlation between signals from two receivers. If we assume a sky signal with random uncorrelated phase, the visibility \mathcal{V}_{12} signal from two identical receivers, located at the position \mathbf{r}_1 and \mathbf{r}_2 can simply be written as a function of their position difference $\Delta \mathbf{r} = \mathbf{r}_1 - \mathbf{r}_2$

$$\mathcal{V}_{12}(\lambda) = \langle s_1(\lambda) s_2(\lambda)^* \rangle = \iint d\Theta I(\Theta, \lambda) L(\Theta, \lambda) e^{i(k_{EM} \cdot \Delta \mathbf{r})} \quad (16)$$

This expression can be simplified if we consider receivers with narrow field of view ($L(\Theta, \lambda) \approx 0$ for $|\Theta| \gtrsim 10^\circ$), and coplanar in respect to their common axis. If we introduce two *Cartesian* like angular coordinates (α, β) centered at the common receivers axis, the visibility would be written as the 2D Fourier transform of the product of the sky intensity and the receiver beam, for the angular frequency $(u, v)_{12} = 2\pi(\frac{\Delta x}{\lambda}, \frac{\Delta y}{\lambda})$:

$$\mathcal{V}_{12}(\lambda) \approx \iint d\alpha d\beta I(\alpha, \beta) L(\alpha, \beta) \exp \left[i2\pi \left(\alpha \frac{\Delta x}{\lambda} + \beta \frac{\Delta y}{\lambda} \right) \right] \quad (17)$$

where $(\Delta x, \Delta y)$ are the two receiver distances on a plane perpendicular to the receiver axis. The x and y axis in the receiver plane are taken parallel to the two (α, β) angular planes.

Furthermore, we introduce the conjugate Fourier variables (u, v) and the Fourier transforms of the sky intensity and the receiver beam:

$$\begin{aligned} (\alpha, \beta) &\longrightarrow (u, v) \\ I(\alpha, \beta, \lambda) &\longrightarrow \mathcal{I}(u, v, \lambda) \\ L(\alpha, \beta, \lambda) &\longrightarrow \mathcal{L}(u, v, \lambda) \end{aligned}$$

The visibility can then be interpreted as the weighted sum of the sky intensity, in an angular wave number domain located around $(u, v)_{12} = 2\pi(\frac{\Delta x}{\lambda}, \frac{\Delta y}{\lambda})$. The weight function is given by the receiver beam Fourier transform.

$$\mathcal{V}_{12}(\lambda) \approx \iint du dv \mathcal{I}(u, v, \lambda) \mathcal{L}(u - 2\pi \frac{\Delta x}{\lambda}, v - 2\pi \frac{\Delta y}{\lambda}, \lambda) \quad (18)$$

A single receiver instrument would measure the total power integrated in a spot centered around the origin in the (u, v) or the angular wave mode plane. The shape of the spot depends on the receiver beam pattern, but its extent would be $\sim 2\pi D/\lambda$, where D is the receiver physical size.

The correlation signal from a pair of receivers would measure the integrated signal on a similar spot, located around the central angular wave mode $(u, v)_{12}$ determined by the relative position of the two receivers (see figure 2). In an interferometer with multiple receivers, the area covered by different receiver pairs in the (u, v) plane might overlap and some pairs might measure the same area (same base lines). Several beams can be formed using different combination of the correlations from a set of antenna pairs.

An instrument can thus be characterized by its (u, v) plane coverage or response $\mathcal{R}(u, v, \lambda)$. For a single dish with a single receiver in the focal plane, the instrument response is simply the Fourier transform of the beam. For a single dish with multiple receivers, either as a Focal Plane Array (FPA) or a multi-horn system, each beam (b) will have its own response $\mathcal{R}_b(u, v, \lambda)$. For an interferometer, we can compute a raw instrument response $\mathcal{R}_{raw}(u, v, \lambda)$ which corresponds to (u, v) plane coverage by all receiver pairs with uniform weighting. Obviously, different weighting schemes can be used, changing the effective beam shape and thus the response $\mathcal{R}_w(u, v, \lambda)$ and the noise behaviour.

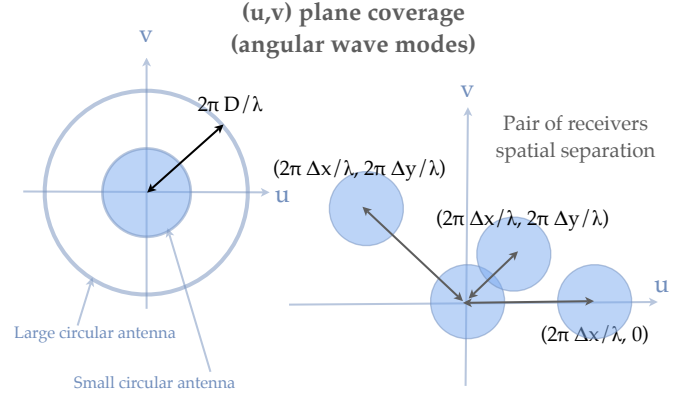


Fig. 2. Schematic view of the (u, v) plane coverage by interferometric measurement.

If the same Fourier angular frequency mode is measured by several receiver pairs, the raw instrument response might then be larger than unity. This non normalized instrument response is used to compute the projected noise power spectrum in the following section (3.3). We can also define a normalized instrument response, $\mathcal{R}_{norm}(u, v, \lambda) \lesssim 1$ as:

$$\mathcal{R}_{norm}(u, v, \lambda) = \mathcal{R}(u, v, \lambda) / \text{Max}_{(u,v)} [\mathcal{R}(u, v, \lambda)] \quad (19)$$

This normalized instrument response can be used to compute the effective instrument beam, in particular in section 4.2.

3.2. Noise power spectrum

Let's consider a total power measurement using a receiver at wavelength λ , over a frequency bandwidth $\delta\nu$ centered on ν_0 , with an integration time t_{int} , characterized by a system temperature T_{sys} . The uncertainty or fluctuations of this measurement due to the receiver noise can be written as $\sigma_{noise}^2 = \frac{2T_{sys}^2}{t_{int}\delta\nu}$. This term corresponds also to the noise for the visibility \mathcal{V}_{12} measured from two identical receivers, with uncorrelated noise. If the receiver has an effective area $A \approx \pi D^2/4$ or $A \approx D_x D_y$, the measurement corresponds to the integration of power over a spot in the angular frequency plane with an area $\sim A/\lambda^2$. The noise spectral density, in the angular frequencies plane (per unit area of angular frequencies $\frac{\delta u}{2\pi} \times \frac{\delta v}{2\pi}$), corresponding to a visibility measurement from a pair of receivers can be written as:

$$P_{noise}^{pair} = \frac{\sigma_{noise}^2}{A/\lambda^2} \quad (20)$$

$$P_{noise}^{pair} \approx \frac{2T_{sys}^2}{t_{int}\delta\nu} \frac{\lambda^2}{D^2} \quad \text{units : K}^2 \times \text{rad}^2 \quad (21)$$

The sky temperature measurement can thus be characterized by the noise spectral power density in the angular frequencies plane $P_{noise}^{(u,v)} \approx \frac{\sigma_{noise}^2}{A/\lambda^2}$, in Kelvin^2 per unit area of angular frequencies $\frac{\delta u}{2\pi} \times \frac{\delta v}{2\pi}$. We can characterize the sky temperature measurement with a radio instrument by the noise spectral power density in the angular frequencies plane $P_{noise}(u, v)$ in units of Kelvin^2 per unit area of angular frequencies $\frac{\delta u}{2\pi} \times \frac{\delta v}{2\pi}$. For an interferometer made of identical receiver elements, several (n) receiver pairs might have the same baseline. The noise power density in the corresponding (u, v) plane area is then reduced by a factor $1/n$. More generally, we can write the instrument noise spectral

power density using the instrument response defined in section 3.1 :

$$P_{noise}(u, v) = \frac{P_{noise}^{pair}}{\mathcal{R}_{raw}(u, v, \lambda)} \quad (22)$$

When the intensity maps are projected in a three dimensional box in the universe and the 3D power spectrum $P(k)$ is computed, angles are translated into comoving transverse distances, and frequencies or wavelengths into comoving radial distance, using the following relations:

$$\delta\alpha, \delta\beta \rightarrow \delta\ell_{\perp} = (1+z)d_A(z)\delta\alpha, \delta\beta \quad (23)$$

$$\delta\nu \rightarrow \delta\ell_{\parallel} = (1+z)\frac{c}{H(z)}\frac{\delta\nu}{\nu} = (1+z)\frac{\lambda}{H(z)}\delta\nu \quad (24)$$

$$\delta u, \delta v \rightarrow \delta k_{\perp} = \frac{\delta u, \delta v}{(1+z)d_A(z)} \quad (25)$$

$$\frac{1}{\delta\nu} \rightarrow \delta k_{\parallel} = \frac{H(z)}{c} \frac{1}{(1+z)} \frac{\nu}{\delta\nu} = \frac{H(z)}{c} \frac{1}{(1+z)^2} \frac{\nu_{21}}{\delta\nu} \quad (26)$$

If we consider a uniform noise spectral density in the (u, v) plane corresponding to the equation 21 above, the three dimensional projected noise spectral density can then be written as:

$$P_{noise}(k) = 2 \frac{T_{sys}^2}{t_{int} \nu_{21}} \frac{\lambda^2}{D^2} d_A^2(z) \frac{c}{H(z)} (1+z)^4 \quad (27)$$

$P_{noise}(k)$ would be in units of $\text{mK}^2 \text{Mpc}^3$ with T_{sys} expressed in mK, t_{int} is the integration time expressed in second, ν_{21} in Hz, c in km/s, d_A in Mpc and $H(z)$ in km/s/Mpc.

The matter or H_I distribution power spectrum determination statistical errors vary as the number of observed Fourier modes, which is inversely proportional to volume of the universe which is observed (sample variance). As the observed volume is proportional to the surveyed solid angle, we consider the survey of a fixed fraction of the sky, defined by total solid angle Ω_{tot} , performed during a determined total observation time t_{obs} . A single dish instrument with diameter D would have an instantaneous field of view $\Omega_{FOV} \sim \left(\frac{\lambda}{D}\right)^2$, and would require a number of pointings $N_{point} = \frac{\Omega_{tot}}{\Omega_{FOV}}$ to cover the survey area. Each sky direction or pixel of size Ω_{FOV} will be observed during an integration time $t_{int} = t_{obs}/N_{point}$. Using equation 27 and the previous expression for the integration time, we can compute a simple expression for the noise spectral power density by a single dish instrument of diameter D :

$$P_{noise}^{survey}(k) = 2 \frac{T_{sys}^2 \Omega_{tot}}{t_{obs} \nu_{21}} d_A^2(z) \frac{c}{H(z)} (1+z)^4 \quad (28)$$

It is important to note that any real instrument do not have a flat response in the (u, v) plane, and the observations provide no information above a certain maximum angular frequency u_{max}, v_{max} . One has to take into account either a damping of the observed sky power spectrum or an increase of the noise spectral power if the observed power spectrum is corrected for damping. The white noise expressions given below should thus be considered as a lower limit or floor of the instrument noise spectral density.

For a single dish instrument of diameter D equipped with a multi-feed or phase array receiver system, with N independent beams on sky, the noise spectral density decreases by a factor N , thanks to the increase of per pointing integration time:

$$P_{noise}^{survey}(k) = \frac{2}{N} \frac{T_{sys}^2 \Omega_{tot}}{t_{obs} \nu_{21}} d_A^2(z) \frac{c}{H(z)} (1+z)^4 \quad (29)$$

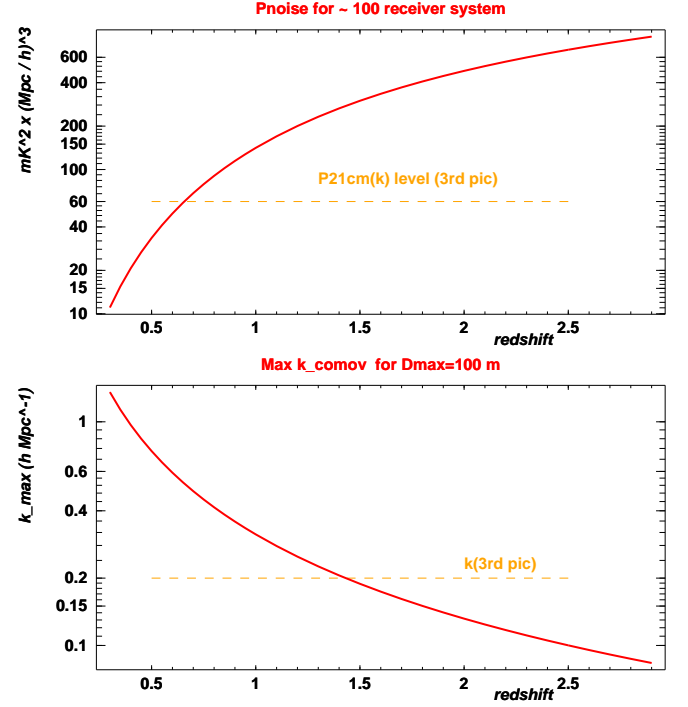


Fig. 3. Minimal noise level for a 100 beams instrument with $T_{sys} = 50\text{K}$ as a function of redshift (top). Maximum k value for a 100 meter diameter primary antenna (bottom)

This expression (eq. 29) can also be used for a filled interferometric array of N identical receivers with a total collection area $\sim D^2$. Such an array could be made for example of $N = q \times q$ *small dishes*, each with diameter D/q , arranged as $q \times q$ square.

For a single dish of diameter D , or an interferometric instrument with maximal extent D , observations provide information up to $u_{max}, v_{max} \lesssim 2\pi D/\lambda$. This value of u_{max}, v_{max} would be mapped to a maximum transverse cosmological wave number k_{max}^{\perp} :

$$k^{\perp} = \frac{(u, v)}{(1+z)d_A} \quad k_{max}^{\perp} \lesssim \frac{2\pi}{d_A (1+z)^2} \frac{D}{\lambda_{21}} \quad (30)$$

Figure 3 shows the evolution of the noise spectral density $P_{noise}^{survey}(k)$ as a function of redshift, for a radio survey of the sky, using an instrument with $N = 100$ beams and a system noise temperature $T_{sys} = 50\text{K}$. The survey is supposed to cover a quarter of sky $\Omega_{tot} = \pi$ rad, in one year. The maximum comoving wave number k_{max} is also shown as a function of redshift, for an instrument with $D = 100\text{m}$ maximum extent. In order to take into account the radial component of \mathbf{k} and the increase of the instrument noise level with k^{\perp} , we have taken the effective k_{max} as half of the maximum transverse k_{max}^{\perp} of eq. 30:

$$k_{max}(z) = \frac{\pi}{d_A (1+z)^2} \frac{D = 100\text{m}}{\lambda_{21}} \quad (31)$$

3.3. Instrument configurations and noise power spectrum

We have numerically computed the instrument response $\mathcal{R}(u, v, \lambda)$ with uniform weights in the (u, v) plane for several instrument configurations:

- a :** A packed array of $n = 121$ $D_{dish} = 5\text{m}$ dishes, arranged in a square 11×11 configuration ($q = 11$). This array covers an area of $55 \times 55 \text{m}^2$

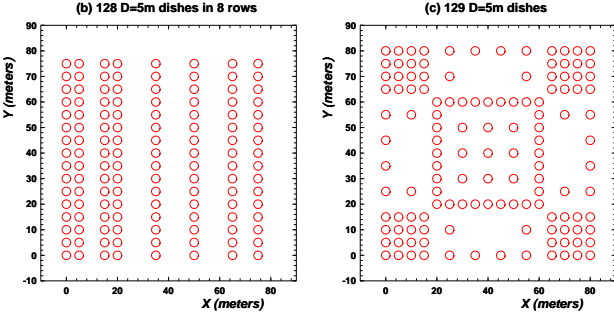


Fig. 4. Array layout for configurations (b) and (c) with 128 and 129 $D=5$ meter diameter dishes.

- b :** An array of $n = 128 D_{dish} = 5$ m dishes, arranged in 8 rows, each with 16 dishes. These 128 dishes are spread over an area $80 \times 80 \text{ m}^2$. The array layout for this configuration is shown in figure 4.
- c :** An array of $n = 129 D_{dish} = 5$ m dishes, arranged over an area $80 \times 80 \text{ m}^2$. This configuration has in particular 4 sub-arrays of packed 16 dishes (4×4), located in the four array corners. This array layout is also shown figure 4.
- d :** A single dish instrument, with diameter $D = 75$ m, equipped with a 100 beam focal plane receiver array.
- e :** A packed array of $n = 400 D_{dish} = 5$ m dishes, arranged in a square 20×20 configuration ($q = 20$). This array covers an area of $100 \times 100 \text{ m}^2$.
- f :** A packed array of 4 cylindrical reflectors, each 85 meter long and 12 meter wide. The focal line of each cylinder is equipped with 100 receivers, each 2λ long, corresponding to ~ 0.85 m at $z = 1$. This array covers an area of $48 \times 85 \text{ m}^2$, and have a total of 400 receivers per polarisation, as in the (e) configuration. We have computed the noise power spectrum for *perfect* cylinders, where all receiver pair correlations are used (fp), or for a non perfect instrument, where only correlations between receivers from different cylinders are used.
- g :** A packed array of 8 cylindrical reflectors, each 102 meter long and 12 meter wide. The focal line of each cylinder is equipped with 120 receivers, each 2λ long, corresponding to ~ 0.85 m at $z = 1$. This array covers an area of $96 \times 102 \text{ m}^2$ and has a total of 960 receivers per polarisation. As for the (f) configuration, we have computed the noise power spectrum for *perfect* cylinders, where all receiver pair correlations are used (gp), or for a non perfect instrument, where only correlations between receivers from different cylinders are used.

We have used simple triangular shaped dish response in the (u, v) plane. However, we have introduced a filling factor or illumination efficiency η , relating the effective dish diameter D_{ill} to the mechanical dish size $D_{dish} = \eta D_{dish}$. The effective area $A_e \propto \eta^2$ scales as η^2 or $\eta_x \eta_y$.

$$\mathcal{L}_o(u, v, \lambda) = \bigwedge_{[\pm 2\pi D_{ill}/\lambda]} (\sqrt{u^2 + v^2}) \quad (32)$$

$$L_o(\alpha, \beta, \lambda) = \left[\frac{\sin(\pi(D_{ill}/\lambda) \sin \theta)}{\pi(D_{ill}/\lambda) \sin \theta} \right]^2 \quad \theta = \sqrt{\alpha^2 + \beta^2} \quad (33)$$

For the multi-dish configuration studied here, we have taken the illumination efficiency factor $\eta = 0.9$.

For the receivers along the focal line of cylinders, we have assumed that the individual receiver response in the (u, v) plane corresponds to one from a rectangular shaped antenna. The illumination efficiency factor has been taken equal to $\eta_x = 0.9$

in the direction of the cylinder width, and $\eta_y = 0.8$ along the cylinder length. It should be noted that the small angle approximation used here for the expression of visibilities is not valid for the receivers along the cylinder axis. However, some preliminary numerical checks indicate that the results obtained here for the noise spectral power density would not change significantly. The instrument responses shown here correspond to fixed pointing toward the zenith, which is the case for a transit type telescope.

$$\mathcal{L}_\square(u, v, \lambda) = \bigwedge_{[\pm 2\pi D_x^{ill}/\lambda]} (u) \times \bigwedge_{[\pm 2\pi D_y^{ill}/\lambda]} (v) \quad (34)$$

Figure 5 shows the instrument response $\mathcal{R}(u, v, \lambda)$ for the four configurations (a,b,c,d) with ~ 100 receivers per polarisation. The resulting projected noise spectral power density is shown in figure 6. The increase of $P_{noise}(k)$ at low $k^{comov} \lesssim 0.02$ is due to the fact that we have ignored all auto-correlation measurements. It can be seen that an instrument with 100–200 beams and $T_{sys} = 50\text{K}$ should have enough sensitivity to map LSS in 21 cm at redshift $z=1$.

4. Foregrounds and Component separation

Reaching the required sensitivities is not the only difficulty of observing the large scale structures in 21 cm. Indeed, the synchrotron emission of the Milky Way and the extra galactic radio sources are a thousand times brighter than the emission of the neutral hydrogen distributed in the universe. Extracting the LSS signal using Intensity Mapping, without identifying the H_I point sources is the main challenge for this novel observation method. Although this task might seem impossible at first, it has been suggested that the smooth frequency dependence of the synchrotron emissions can be used to separate the faint LSS signal from the Galactic and radio source emissions. However, any real radio instrument has a beam shape which changes with frequency: this instrumental effect significantly increases the difficulty and complexity of this component separation technique. The effect of frequency dependent beam shape is some time referred to as *mode mixing*. See for example (Morales et al. (2006)), (Bowman et al. (2009)).

In this section, we present a short description of the foreground emissions and the simple models we have used for computing the sky radio emissions in the GHz frequency range. We present also a simple component separation method to extract the LSS signal and its performance. We show in particular the effect of the instrument response on the recovered power spectrum. The results presented in this section concern the total sky emission and the LSS 21 cm signal extraction in the $z \sim 0.6$ redshift range, corresponding to the central frequency $\nu \sim 884$ MHz.

4.1. Synchrotron and radio sources

We have modeled the radio sky in the form of three dimensional maps (data cubes) of sky temperature brightness $T(\alpha, \delta, \nu)$ as a function of two equatorial angular coordinates (α, δ) and the frequency ν . Unless otherwise specified, the results presented here are based on simulations of $90 \times 30 \approx 2500 \text{ deg}^2$ of the sky, centered on $\alpha = 10\text{h}00\text{m}$, $\delta = +10 \text{ deg.}$, and covering 128 MHz in frequency. We have selected this particular area of the sky in order to minimize the Galactic synchrotron foreground. The sky cube characteristics (coordinate range, size, resolution) used in the simulations are given in the table 3.

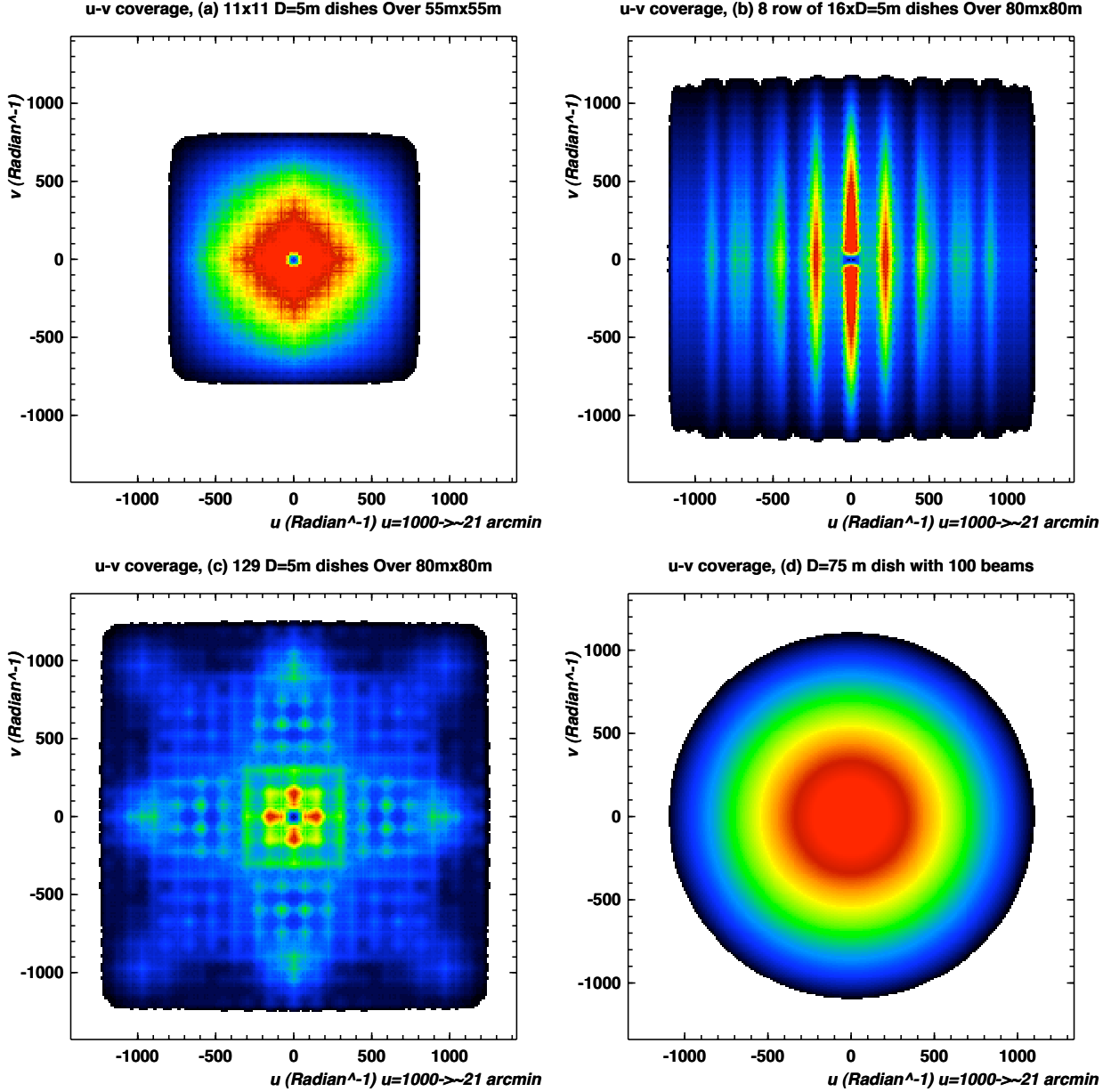


Fig. 5. (u, v) plane coverage (raw instrument response $\mathcal{R}(u, v, \lambda)$) for four configurations. (a) 121 $D_{dish} = 5$ meter diameter dishes arranged in a compact, square array of 11×11 , (b) 128 dishes arranged in 8 row of 16 dishes each (fig. 4), (c) 129 dishes arranged as shown in figure 4, (d) single $D=75$ meter diameter, with 100 beams. (color scale : black < 1 , blue, green, yellow, red $\gtrsim 80$)

Two different methods have been used to compute the sky temperature data cubes. We have used the Global Sky Model (GSM) (Oliveira-Costa et al. (2008)) tools to generate full sky maps of the emission temperature at different frequencies, from which we have extracted the brightness temperature cube for the region defined above (Model-I/GSM $T_{gsm}(\alpha, \delta, \nu)$). As the GSM maps have an intrinsic resolution of ~ 0.5 degree, it is difficult to have reliable results for the effect of point sources on the reconstructed LSS power spectrum.

We have thus made also a simple sky model using the Haslam Galactic synchrotron map at 408 MHz (Haslam et al. (1982)) and the NRAO VLA Sky Survey (NVSS) 1.4 GHz radio source catalog (Condon et al. (1998)). The sky temperature cube in this model (Model-II/Haslam+NVSS) has been computed through the following steps:

1. The Galactic synchrotron emission is modeled as a power law with spatially varying spectral index. We assign a power law index $\beta = -2.8 \pm 0.15$ to each sky direction. β has a gaussian distribution centered at -2.8 and with standard deviation $\sigma_\beta = 0.15$. The synchrotron contribution to the sky temperature for each cell is then obtained through the formula:

$$T_{sync}(\alpha, \delta, \nu) = T_{haslam} \times \left(\frac{\nu}{408 \text{ MHz}} \right)^\beta$$

2. A two dimensional $T_{nvss}(\alpha, \delta)$ sky brightness temperature at 1.4 GHz is computed by projecting the radio sources in the NVSS catalog to a grid with the same angular resolution as the sky cubes. The source brightness in Jansky is converted to temperature taking the pixel angular size into account ($\sim 21 \text{ mK/mJansky}$ at 1.4 GHz and $3' \times 3'$ pixels). A spectral index $\beta_{src} \in [-1.5, -2]$ is also assigned to each sky direction

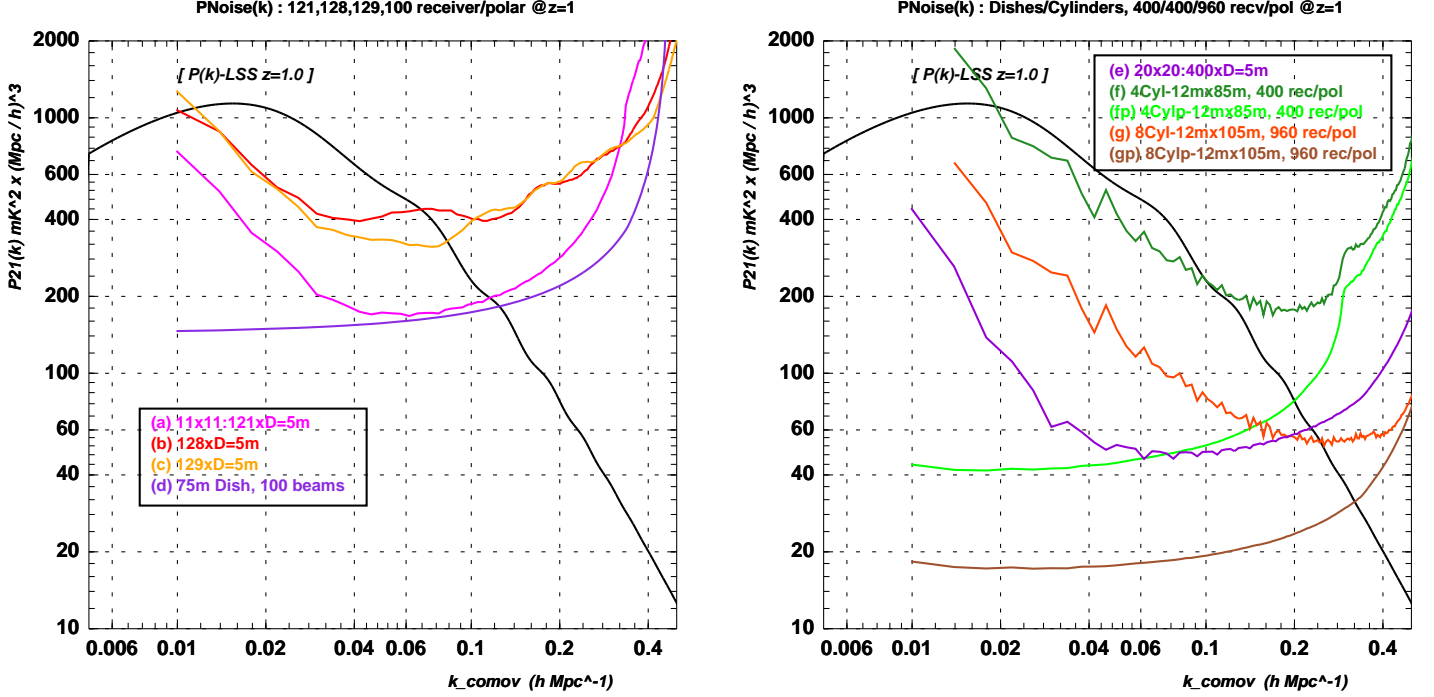


Fig. 6. $P(k)$ LSS power and noise power spectrum for several interferometer configurations ((a),(b),(c),(d),(e),(f),(g)) with 121, 128, 129, 400 and 960 receivers.

	range	center
Right ascension	$105 < \alpha < 195$ deg.	150 deg.
Declination	$-5 < \delta < 25$ deg.	+10 deg.
Frequency	$820 < \nu < 948$ MHz	884 MHz
Wavelength	$36.6 < \lambda < 31.6$ cm	33.9 cm
Redshift	$0.73 < z < 0.5$	0.61
	resolution	N-cells
Right ascension	3 arcmin	1800
Declination	3 arcmin	600
Frequency	500 kHz ($dz \sim 10^{-3}$)	256

Table 3. Sky cube characteristics for the simulation performed in this paper. Cube size : 90 deg. \times 30 deg. \times 128 MHz 1800 \times 600 \times 256 \simeq 123 10^6 cells

for the radio source map; we have taken β_{src} as a flat random number in the range $[-1.5, -2]$, and the contribution of the radiosources to the sky temperature is computed as follows:

$$T_{radsrc}(\alpha, \delta, \nu) = T_{nvss} \times \left(\frac{\nu}{1420 \text{ MHz}} \right)^{\beta_{src}}$$

3. The sky brightness temperature data cube is obtained through the sum of the two contributions, Galactic synchrotron and resolved radio sources:

$$T_{fgnd}(\alpha, \delta, \nu) = T_{sync}(\alpha, \delta, \nu) + T_{radsrc}(\alpha, \delta, \nu)$$

The 21 cm temperature fluctuations due to neutral hydrogen in large scale structures $T_{lss}(\alpha, \delta, \nu)$ have been computed using the SimLSS¹ software package: complex normal Gaussian fields were first generated in Fourier space. The amplitude of each

mode was then multiplied by the square root of the power spectrum $P(k)$ at $z = 0$ computed according to the parametrization of (Eisenstein & Hu (1998)). We have used the standard cosmological parameters, $H_0 = 71$ km/s/Mpc, $\Omega_m = 0.27$, $\Omega_b = 0.044$, $\Omega_\Lambda = 0.73$ and $w = -1$. An inverse FFT was then performed to compute the matter density fluctuations $\delta\rho/\rho$ in the linear regime, in a box of $3420 \times 1140 \times 716 \text{ Mpc}^3$ and evolved to redshift $z = 0.6$. The size of the box is about 2500 deg^2 in the transverse direction and $\Delta z \simeq 0.23$ in the longitudinal direction. The size of the cells is $1.9 \times 1.9 \times 2.8 \text{ Mpc}^3$, which correspond approximately to the sky cube angular and frequency resolution defined above.

The mass fluctuations has been converted into temperature through a factor 0.13 mK, corresponding to a hydrogen fraction $0.008 \times (1 + 0.6)$, using equation 10. The total sky brightness temperature is then computed as the sum of foregrounds and the LSS 21 cm emission:

$$T_{sky} = T_{sync} + T_{radsrc} + T_{lss} \quad \text{OR} \quad T_{sky} = T_{gsm} + T_{lss}$$

Table 4 summarizes the mean and standard deviation of the sky brightness temperature $T(\alpha, \delta, \nu)$ for the different components computed in this study. It should be noted that the standard deviation depends on the map resolution and the values given in table 4 correspond to sky cubes computed here, with ~ 3 arc minute angular and 500 kHz frequency resolutions (see table 3). Figure 8 shows the comparison of the GSM temperature map at 884 MHz with Haslam+NVSS map, smoothed with a 35 arcmin gaussian beam. Figure 7 shows the comparison of the sky cube temperature distribution for Model-I/GSM and Model-II. There is good agreement between the two models, although the mean temperature for Model-II is slightly higher ($\sim 10\%$) than Model-I.

¹ SimLSS : <http://www.sophya.org/SimLSS>

	mean (K)	std.dev (K)
Haslam	2.17	0.6
NVSS	0.13	7.73
Haslam+NVSS	2.3	7.75
(Haslam+NVSS)*Lobe(35')	2.3	0.72
GSM	2.1	0.8

Table 4. Mean temperature and standard deviation for the different sky brightness data cubes computed for this study (see table 3 for sky cube resolution and size).

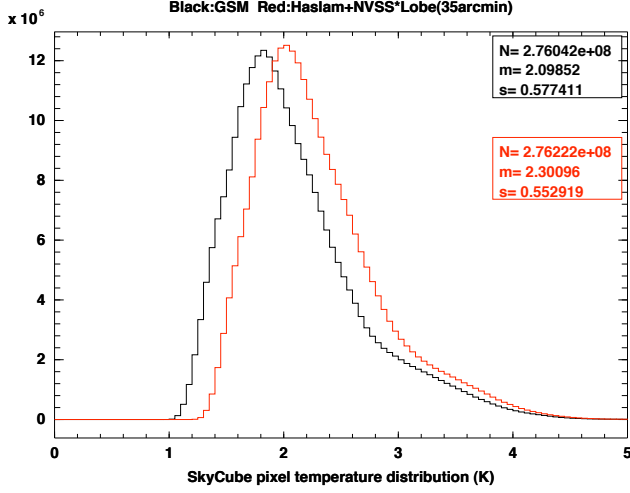


Fig. 7. Comparison of GSM (black) Model-II (red) sky cube temperature distribution. The Model-II (Haslam+NVSS), has been smoothed with a 35 arcmin gaussian beam.

we have computed the power spectrum for the 21cm-LSS sky temperature cube, as well as for the radio foreground temperature cubes obtained from the two models. We have also computed the power spectrum on sky brightness temperature cubes, as measured by a perfect instrument having a 25 arcmin (FWHM) gaussian beam. The resulting computed power spectra are shown on figure 9. The GSM model has more large scale power compared to our simple Haslam+NVSS model, while it lacks power at higher spatial frequencies. The mode mixing due to frequency dependent response will thus be stronger in Model-II (Haslam+NVSS) case. It can also be seen that the radio foreground power spectrum is more than $\sim 10^6$ times higher than the 21 cm signal from large scale structures. This corresponds to the factor $\sim 10^3$ of the sky brightness temperature fluctuations (\sim K), compared to the mK LSS signal.

It should also be noted that in section 3, we presented the different instrument configuration noise levels after *correcting or deconvolving* the instrument response. The LSS power spectrum is recovered unaffected in this case, while the noise power spectrum increases at high k values (small scales). In practice, clean deconvolution is difficult to implement for real data and the power spectra presented in this section are NOT corrected for the instrumental response. The observed structures have thus a scale dependent damping according to the instrument response, while the instrument noise is flat (white noise or scale independent).

4.2. Instrument response and LSS signal extraction

The *observed* data cube is obtained from the sky brightness temperature 3D map $T_{sky}(\alpha, \delta, \nu)$ by applying the frequency or wave-

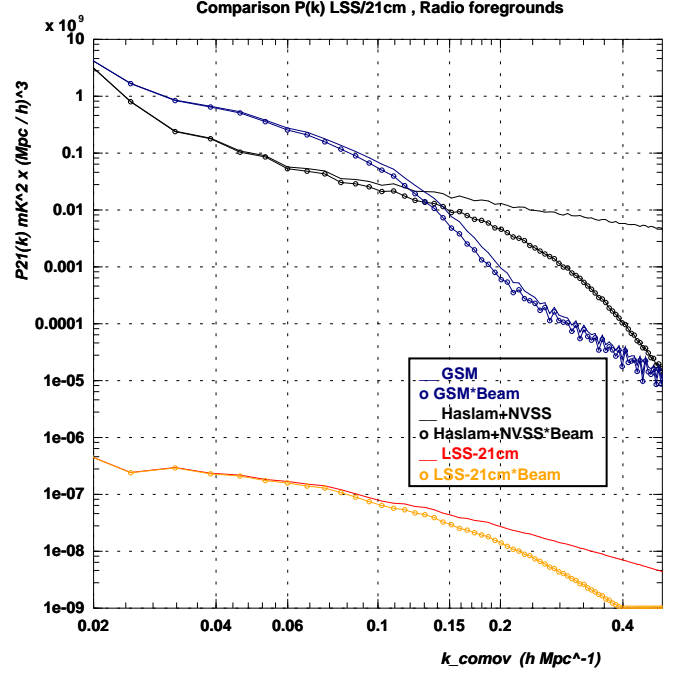


Fig. 9. Comparison of the 21cm LSS power spectrum (red, orange) with the radio foreground power spectrum. The radio sky power spectrum is shown for the GSM (Model-I) sky model (dark blue), as well as for our simple model based on Haslam+NVSS (Model-II, black). The curves with circle markers show the power spectrum as observed by a perfect instrument with a 25 arcmin (FWHM) gaussian beam.

length dependent instrument response $\mathcal{R}(u, v, \lambda)$. We have considered the simple case where the instrument response is constant throughout the survey area, or independent of the sky direction. For each frequency ν_k or wavelength $\lambda_k = c/\nu_k$:

1. Apply a 2D Fourier transform to compute sky angular Fourier amplitudes

$$T_{sky}(\alpha, \delta, \lambda_k) \rightarrow \text{2D - FFT} \rightarrow \mathcal{T}_{sky}(u, v, \lambda_k)$$

2. Apply instrument response in the angular wave mode plane. We use here the normalized instrument response $\mathcal{R}(u, v, \lambda_k) \lesssim 1$.

$$\mathcal{T}_{sky}(u, v, \lambda_k) \rightarrow \mathcal{T}_{sky}(u, v, \lambda_k) \times \mathcal{R}(u, v, \lambda_k)$$

3. Apply inverse 2D Fourier transform to compute the measured sky brightness temperature map, without instrumental (electronic/ T_{sys}) white noise:

$$\mathcal{T}_{sky}(u, v, \lambda_k) \times \mathcal{R}(u, v, \lambda_k) \rightarrow \text{Inv - 2D - FFT} \rightarrow T_{mes1}(\alpha, \delta, \lambda_k)$$

4. Add white noise (gaussian fluctuations) to the pixel map temperatures to obtain the measured sky brightness temperature $T_{mes}(\alpha, \delta, \nu_k)$. We have also considered that the system temperature and thus the additive white noise level was independent of the frequency or wavelength.

The LSS signal extraction depends indeed on the white noise level. The results shown here correspond to the (a) instrument configuration, a packed array of $11 \times 11 = 121$ dishes (5 meter diameter), with a white noise level corresponding to $\sigma_{noise} = 0.25$ mK per $3 \times 3 \text{ arcmin}^2 \times 500 \text{ kHz}$ cell.

A brief description of the simple component separation procedure that we have applied is given here:

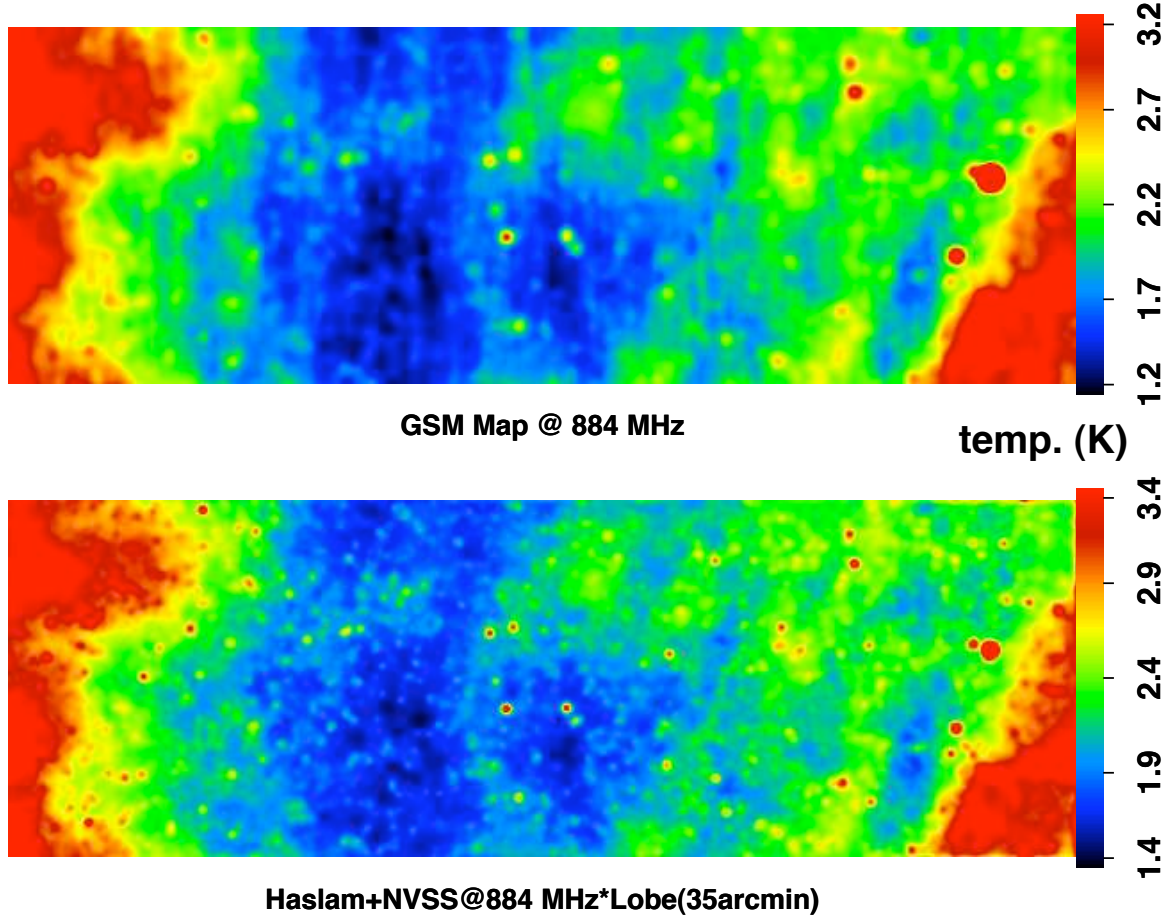


Fig. 8. Comparison of GSM map (top) and Model-II sky map at 884 MHz (bottom). The Model-II (Haslam+NVSS) has been smoothed with a 35 arcmin (FWHM) gaussian beam.

1. The measured sky brightness temperature is first *corrected* for the frequency dependent beam effects through a convolution by a fiducial frequency independent beam. This *correction* corresponds to a smearing or degradation of the angular resolution. We assume that we have a perfect knowledge of the intrinsic instrument response, up to a threshold numerical level of about $\gtrsim 1\%$ for $\mathcal{R}(u, v, \lambda)$. We recall that this is the normalized instrument response, $\mathcal{R}(u, v, \lambda) \lesssim 1$.

$$T_{mes}(\alpha, \delta, \nu) \longrightarrow T_{mes}^{bcor}(\alpha, \delta, \nu)$$

The virtual target instrument has a beam width larger than the worst real instrument beam, i.e at the lowest observed frequency.

2. For each sky direction (α, δ) , a power law $T = T_0 \left(\frac{\nu}{\nu_0}\right)^b$ is fitted to the beam-corrected brightness temperature. The fit is done through a linear χ^2 fit in the $\log_{10}(T)$, $\log_{10}(\nu)$ plane and we show here the results for a pure power law (P1) or modified power law (P2):

$$P1 : \log_{10}(T_{mes}^{bcor}(\nu)) = a + b \log_{10}(\nu/\nu_0)$$

$$P2 : \log_{10}(T_{mes}^{bcor}(\nu)) = a + b \log_{10}(\nu/\nu_0) + c \log_{10}(\nu/\nu_0)^2$$

where b is the power law index and $T_0 = 10^a$ is the brightness temperature at the reference frequency ν_0 :

3. The difference between the beam-corrected sky temperature and the fitted power law ($T_0(\alpha, \delta)$, $b(\alpha, \delta)$) is our extracted 21 cm LSS signal.

Figure 10 shows the performance of this procedure at a redshift ~ 0.6 , for the two radio sky models used here: GSM/Model-I and Haslam+NVSS/Model-II. The 21 cm LSS power spectrum, as seen by a perfect instrument with a 25 arcmin (FWHM) gaussian frequency independent beam is shown in orange (solid line), and the extracted power spectrum, after beam *correction* and foreground separation with second order polynomial fit (P2) is shown in red (circle markers). We have also represented the obtained power spectrum without applying the beam correction (step 1 above), or with the first order polynomial fit (P1).

Figure 11 shows a comparison of the original 21 cm brightness temperature map at 884 MHz with the recovered 21 cm map, after subtraction of the radio continuum component. It can be seen that structures present in the original map have been correctly recovered, although the amplitude of the temperature fluctuations on the recovered map is significantly smaller (factor ~ 5) than in the original map. This is mostly due to the damping of the large scale ($k \lesssim 0.04 h \text{Mpc}^{-1}$) due the poor interferometer response at large angle ($\theta \gtrsim 4^\circ$).

We have shown that it should be possible to measure the red shifted 21 cm emission fluctuations in the presence of the strong radio continuum signal, provided that this latter has a smooth frequency dependence. However, a rather precise knowledge of the instrument beam and the beam *correction* or smearing procedure described here are key ingredient for recovering the 21 cm LSS power spectrum. It is also important to note that while it is enough to correct the beam to the lowest resolution instru-

ment beam ($\sim 30'$ or $D \sim 50$ meter @ 820 MHz) for the GSM sky model, a stronger beam correction has to be applied ($\sim 36'$ or $D \sim 40$ meter @ 820 MHz) for the Model-II to reduce significantly the ripples from bright radio sources. We have also applied the same procedure to simulate observations and LSS signal extraction for an instrument with a frequency dependent gaussian beam shape. The mode mixing effect is greatly reduced for such a smooth beam, compared to the more complex instrument response $\mathcal{R}(u, v, \lambda)$ used for the results shown in figure 10.

4.3. $P_{21}(k)$ measurement transfer function

The recovered red shifted 21 cm emission power spectrum $P_{21}^{rec}(k)$ suffers a number of distortions, mostly damping, compared to the original $P_{21}(k)$ due to the instrument response and the component separation procedure. We expect damping at small scales, or large k , due to the finite instrument size, but also at large scales, small k , if total power measurements (auto-correlations) are not used in the case of interferometers. The sky reconstruction and the component separation introduce additional filtering and distortions. Ideally, one has to define a power spectrum measurement response or *transfer function* in the radial direction, (λ or redshift, $\mathbf{T}(k_{||})$) and in the transverse plane ($\mathbf{T}(k_{\perp})$). The real transverse plane transfer function might even be anisotropic.

However, in the scope of the present study, we define an overall transfer function $\mathbf{T}(k)$ as the ratio of the recovered 3D power spectrum $P_{21}^{rec}(k)$ to the original $P_{21}(k)$:

$$\mathbf{T}(k) = P_{21}^{rec}(k)/P_{21}(k) \quad (35)$$

Figure 12 shows this overall transfer function for the simulations and component separation performed here, around $z \sim 0.6$, for the instrumental setup (a), a filled array of 121 $D_{dish} = 5$ m dishes. The orange/yellow curve shows the ratio $P_{21}^{smoothed}(k)/P_{21}(k)$ of the computed to the original power spectrum, if the original LSS temperature cube is smoothed by the frequency independent target beam FWHM=30' for the GSM simulations (left), 36' for Model-II (right). This orange/yellow curve shows the damping effect due to the finite instrument size at small scales ($k \gtrsim 0.1 h \text{ Mpc}^{-1}$, $\theta \lesssim 1^\circ$). The recovered power spectrum suffers also significant damping at large scales $k \lesssim 0.05 h \text{ Mpc}^{-1}$, due to poor interferometer response at large angles ($\theta \gtrsim 4^\circ - 5^\circ$), as well as to the filtering of radial or longitudinal Fourier modes along the frequency or redshift direction ($k_{||}$) by the component separation algorithm. The red curve shows the ratio of $P(k)$ computed on the recovered or extracted 21 cm LSS signal, to the original LSS temperature cube $P_{21}^{rec}(k)/P_{21}(k)$ and corresponds to the transfer function $\mathbf{T}(k)$ defined above, for $z = 0.6$ and instrument setup (a). The black (thin line) curve shows the ratio of recovered to the smoothed power spectrum $P_{21}^{rec}(k)/P_{21}^{smoothed}(k)$. This latter ratio (black curve) exceeds one for $k \gtrsim 0.2$, which is due to the noise or system temperature. It should be stressed that the simulations presented in this section were focused on the study of the radio foreground effects and have been carried intently with a very low instrumental noise level of 0.25 mK per pixel, corresponding to several years of continuous observations (~ 10 hours per $3' \times 3'$ pixel).

This transfer function is well represented by the analytical form:

$$\mathbf{T}(k) = \sqrt{\frac{k - k_A}{k_B}} \times \exp\left(-\frac{k}{k_C}\right) \quad (36)$$

We have performed simulation of observations and radio foreground subtraction using the procedure described here for

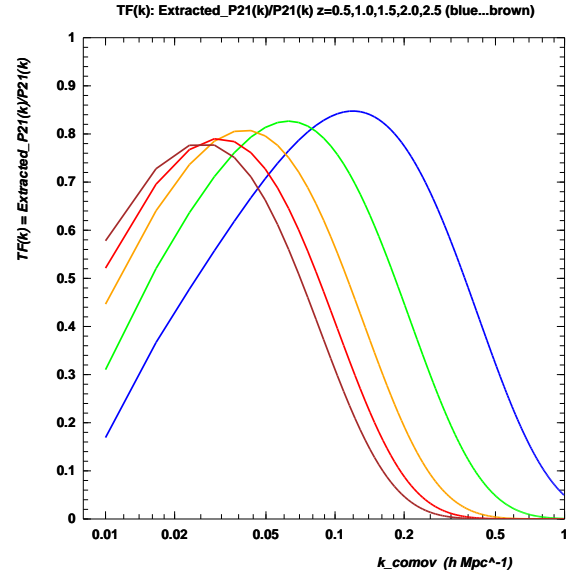


Fig. 13. Fitted/smoothed transfer function $\mathbf{T}(k)$ obtained for the recovered 21 cm power spectrum at different redshifts, $z = 0.5, 1.0, 1.5, 2.0, 2.5$ for the instrument configuration (e), 20×20 packed array interferometer.

different redshifts and instrument configurations, in particular for the (e) configuration with 400 five-meter dishes. As the synchrotron and radio source strength increases quickly with decreasing frequency, we have seen that recovering the 21 cm LSS signal becomes difficult for larger redshifts, in particular for $z \gtrsim 2$.

We have determined the transfer function parameters of eq. 36 k_A, k_B, k_C for setup (e) for three redshifts, $z = 0.5, 1, 1.5$, and then extrapolated the value of the parameters for redshift $z = 2, 2.5$. The value of the parameters are grouped in table 5 and the smoothed transfer functions are shown on figure 13.

z	0.5	1.0	1.5	2.0	2.5
k_A	0.006	0.005	0.004	0.0035	0.003
k_B	0.038	0.019	0.012	0.0093	0.008
k_C	0.16	0.08	0.05	0.038	0.032

Table 5. Value of the parameters for the transfer function (eq. 36) at different redshift for instrumental setup (e), 20×20 packed array interferometer.

5. Sensitivity to cosmological parameters

The impact of the various telescope configurations on the sensitivity for 21 cm power spectrum measurement has been discussed in section 3. Fig. 6 shows the noise power spectra, and allows us to rank visually the configurations in terms of instrument noise contribution to $P(k)$ measurement. The differences in P_{noise} will translate into differing precisions in the reconstruction of the BAO peak positions and in the estimation of cosmological parameters. In addition, we have seen (sec. 4.2) that subtraction of continuum radio emissions, Galactic synchrotron and radio sources, has also an effect on the measured 21 cm power spectrum. In this paragraph, we present our method and the results

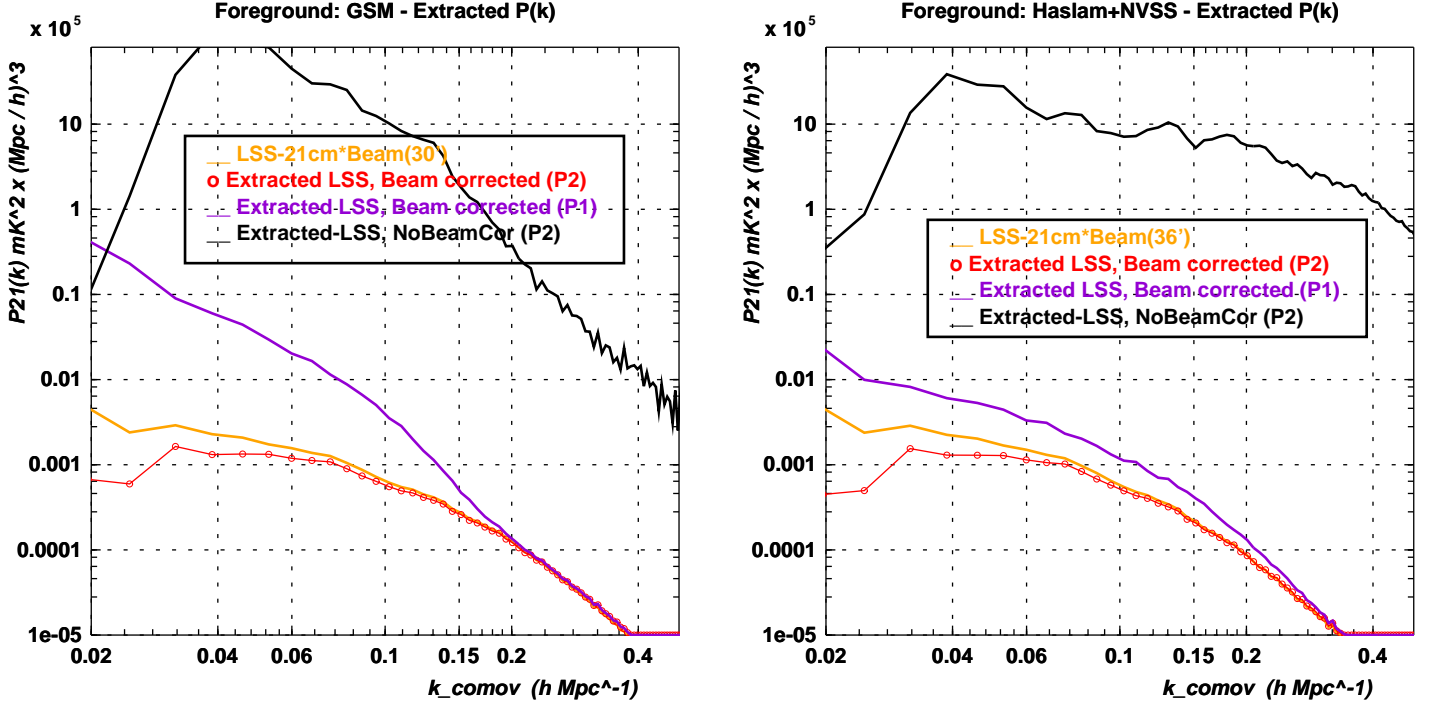


Fig. 10. Recovered power spectrum of the 21cm LSS temperature fluctuations, separated from the continuum radio emissions at $z \sim 0.6$, for the instrument configuration (a), 11×11 packed array interferometer. Left: GSM/Model-I, right: Haslam+NVSS/Model-II. black curve shows the residual after foreground subtraction, corresponding to the 21 cm signal, WITHOUT applying the beam correction. Red curve shows the recovered 21 cm signal power spectrum, for P2 type fit of the frequency dependence of the radio continuum, and violet curve is the P1 fit (see text). The orange/yellow curve shows the original 21 cm signal power spectrum, smoothed with a perfect, frequency independent gaussian beam.

for the precisions on the estimation of Dark Energy parameters, through a radio survey of the redshifted 21 cm emission of LSS, with an instrumental setup similar to the (e) configuration (sec. 3.3), 400 five-meter diameter dishes, arranged into a filled 20×20 array.

5.1. BAO peak precision

In order to estimate the precision with which BAO peak positions can be measured, we used a method similar to the one established in (Blake and Glazebrook (2003)) and (Glazebrook and Blake (2005)).

To this end, we generated reconstructed power spectra $P^{rec}(k)$ for slices of Universe with a quarter-sky coverage and a redshift depth, $\Delta z = 0.5$ for $0.25 < z < 2.75$. The peaks in the generated spectra were then determined by a fitting procedure and the reconstructed peak positions compared with the generated peak positions. The reconstructed power spectrum used in the simulation is the sum of the expected H_I signal term, corresponding to equations 9 and 10, damped by the transfer function $\mathbf{T}(k)$ (Eq. 36, table 5) and a white noise component P_{noise} calculated according to the equation 29, established in section 3.3 with $N = 400$:

$$P^{rec}(k) = P_{21}(k) \times \mathbf{T}(k) + P_{noise} \quad (37)$$

where the different terms ($P_{21}(k)$, $\mathbf{T}(k)$, P_{noise}) depend on the slice redshift. The expected 21 cm power spectrum $P_{21}(k)$ has

been generated according to the formula:

$$\frac{P_{21}(k_{\perp}, k_{\parallel})}{P_{ref}(k_{\perp}, k_{\parallel})} = 1 + A k \exp(-(k/\tau)^{\alpha}) \sin \left(2\pi \sqrt{\frac{k_{\perp}^2}{k_{BAO\perp}^2} + \frac{k_{\parallel}^2}{k_{BAO\parallel}^2}} \right) \quad (38)$$

where $k = \sqrt{k_{\perp}^2 + k_{\parallel}^2}$, the parameters A , α and τ are adjusted to the formula presented in (Eisenstein & Hu (1998)). $P_{ref}(k_{\perp}, k_{\parallel})$ is the envelop curve of the HI power spectrum without baryonic oscillations. The parameters $k_{BAO\perp}$ and $k_{BAO\parallel}$ are the inverses of the oscillation periods in k -space. The following values have been used for these parameters for the results presented here: $A = 1.0$, $\tau = 0.1 \text{ h Mpc}^{-1}$, $\alpha = 1.4$ and $k_{BAO\perp} = k_{BAO\parallel} = 0.060 \text{ h Mpc}^{-1}$.

Each simulation is performed for a given set of parameters which are: the system temperature, T_{sys} , an observation time, t_{obs} , an average redshift and a redshift depth, $\Delta z = 0.5$. Then, each simulated power spectrum is fitted with a two dimensional normalized function $P_{tot}(k_{\perp}, k_{\parallel})/P_{ref}(k_{\perp}, k_{\parallel})$ which is the sum of the signal power spectrum damped by the transfer function and the noise power spectrum multiplied by a linear term, $a_0 + a_1 k$. The upper limit k_{max} in k of the fit corresponds to the approximate position of the linear/non-linear transition. This limit is established on the basis of the criterion discussed in (Blake and Glazebrook (2003)). In practice,

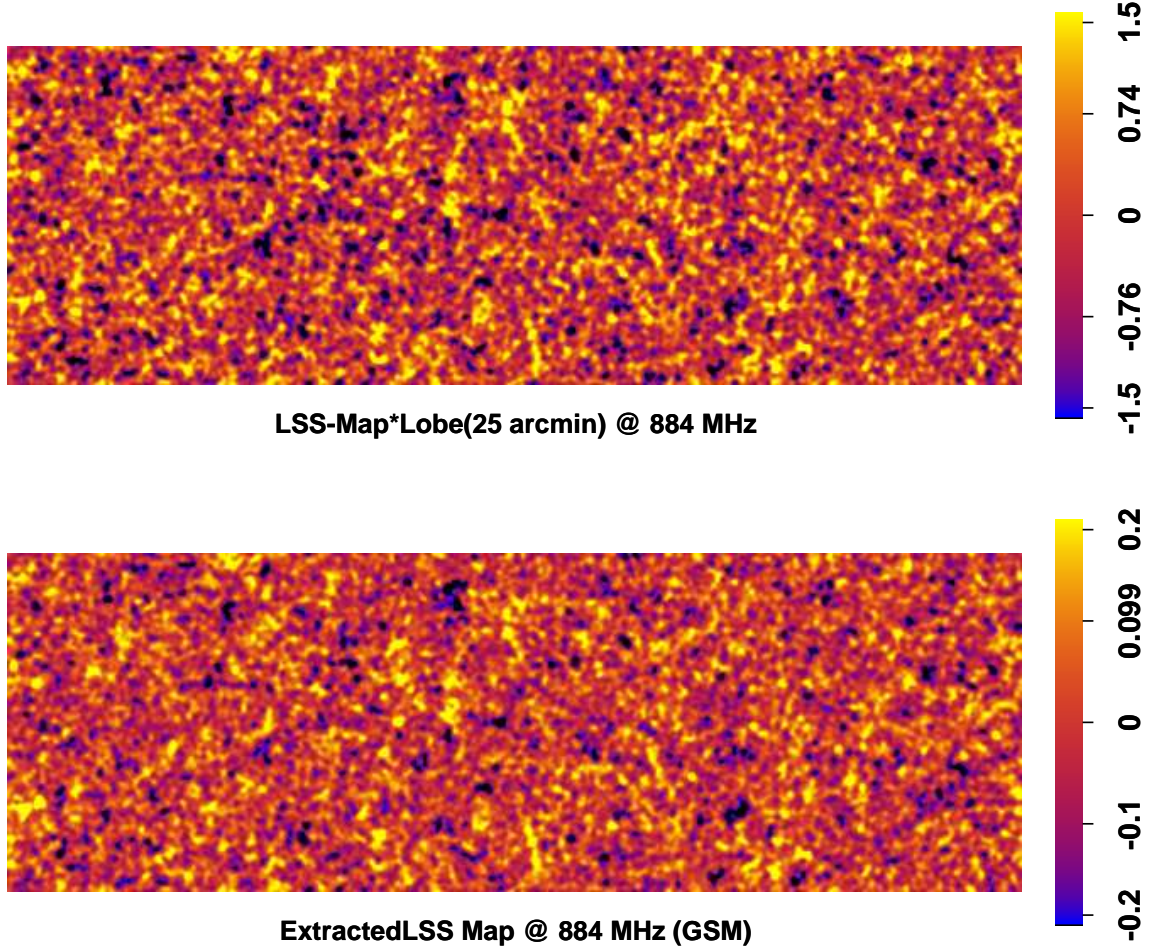


Fig. 11. Comparison of the original 21 cm LSS temperature map @ 884 MHz ($z \sim 0.6$), smoothed with 25 arcmin (FWHM) beam (top), and the recovered LSS map, after foreground subtraction for Model-I (GSM) (bottom), for the instrument configuration (a), 11×11 packed array interferometer. Notice the difference between the temperature color scales (mK) for the top and bottom maps.

we used for the redshifts $z = 0.5, 1.0$ and 1.5 respectively $k_{max} = 0.145 h \text{ Mpc}^{-1}$, $0.18 h \text{ Mpc}^{-1}$ and $0.23 h \text{ Mpc}^{-1}$.

Figure 14 shows the result of the fit for one of these simulations. Figure 15 histograms the recovered values of $k_{BAO\perp}$ and $k_{BAO\parallel}$ for 100 simulations. The widths of the two distributions give an estimate of the statistical errors.

In addition, in the fitting procedure, both the parameters modeling the signal A , τ , α and the parameter correcting the noise power spectrum (a_0, a_1) are floated to take into account the possible ignorance of the signal shape and the uncertainties in the computation of the noise power spectrum. In this way, we can correct possible imperfections and the systematic uncertainties are directly propagated to statistical errors on the relevant parameters $k_{BAO\perp}$ and $k_{BAO\parallel}$. By subtracting the fitted noise contribution to each simulation, the baryonic oscillations are clearly observed, for instance, on Fig. 16.

In our comparison of the various configurations, we have considered the following cases for $\Delta z = 0.5$ slices with $0.25 < z < 2.75$.

- *Simulation without electronics noise:* the statistical errors on the power spectrum are directly related to the number of modes in the surveyed volume V corresponding to $\Delta z = 0.5$ slice with the solid angle $\Omega_{tot} = 1 \pi$ sr. The number of mode

z	0.5	1.0	1.5	2.0	2.5
$P_{noise} \text{ mK}^2 (\text{Mpc}/h)^3$	8.5	35	75	120	170

Table 6. Instrument or electronic noise spectral power P_{noise} for a $N = 400$ dish interferometer with $T_{sys} = 50 \text{ K}$ and $t_{obs} = 1$ year to survey $\Omega_{tot} = \pi$ sr

$N_{\delta k}$ in the wave number interval δk can be written as:

$$V = \frac{c}{H(z)} \Delta z \times (1+z)^2 d_A^2 \Omega_{tot} \quad N_{\delta k} = \frac{V}{4\pi^2} k^2 \delta k \quad (39)$$

- *Noise:* we add the instrument noise as a constant term P_{noise} as described in Eq. 29. Table 6 gives the white noise level for $T_{sys} = 50 \text{ K}$ and one year total observation time to survey $\Omega_{tot} = 1 \pi$ sr.
- *Noise with transfer function:* we take into account of the interferometer and radio foreground subtraction represented as the measured $P(k)$ transfer function $T(k)$ (section 4.3), as well as instrument noise P_{noise} .

Table 7 summarizes the result. The errors both on $k_{BAO\perp}$ and $k_{BAO\parallel}$ decrease as a function of redshift for simulations without electronic noise because the volume of the universe probed is larger. Once we apply the electronics noise, each slice in redshift give comparable results. Finally, after applying the full re-

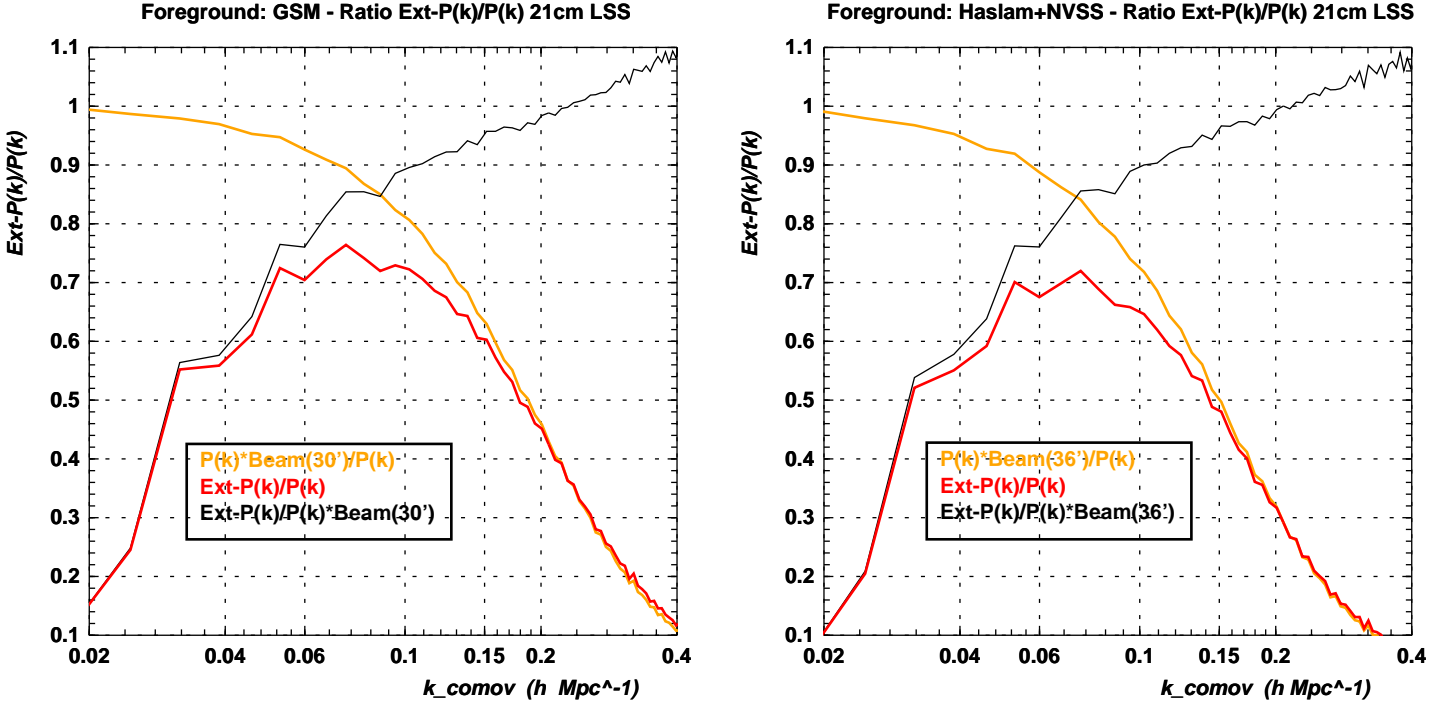


Fig. 12. Ratio of the reconstructed or extracted 21cm power spectrum, after foreground removal, to the initial 21 cm power spectrum, $T(k) = P_{21}^{rec}(k)/P_{21}(k)$, at $z \sim 0.6$, for the instrument configuration (a), 11×11 packed array interferometer. Left: GSM/Model-I, right: Haslam+NVSS/Model-II.

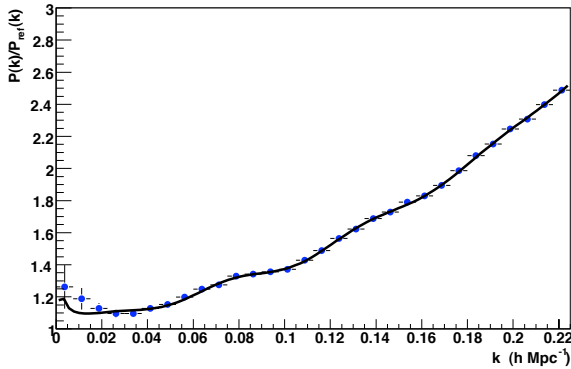


Fig. 14. 1D projection of the power spectrum for one simulation. The H_I power spectrum is divided by an envelop curve $P(k)_{ref}$ corresponding to the power spectrum without baryonic oscillations. The dots represent one simulation for a "packed" array of cylinders with a system temperature, $T_{sys} = 50K$, an observation time, $T_{obs} = 1$ year, a solid angle of $1\pi sr$, an average redshift, $z = 1.5$ and a redshift depth, $\Delta z = 0.5$. The solid line is the result of the fit to the data.

construction of the interferometer, the best accuracy is obtained for the first slices in redshift around 0.5 and 1.0 for an identical time of observation. We can optimize the survey by using a different observation time for each slice in redshift. Finally, for a 3 year survey we can split in five observation periods with durations which are 3 months, 3 months, 6 months, 1 year and 1 year respectively for redshift 0.5, 1.0, 1.5, 2.0 and 2.5.

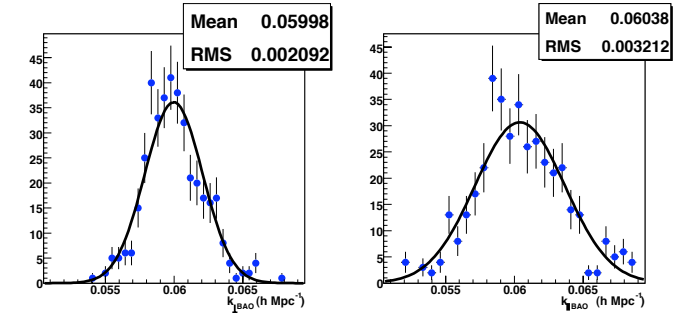


Fig. 15. Distributions of the reconstructed wavelength $k_{BAO\perp}$ and $k_{BAO\parallel}$ respectively, perpendicular and parallel to the line of sight for simulations as in Fig. 14. The fit by a Gaussian of the distribution (solid line) gives the width of the distribution which represents the statistical error expected on these parameters.

5.2. Expected sensitivity on w_0 and w_a

The observations give the H_I power spectrum in angle-angle-redshift space rather than in real space. The inverse of the peak positions in the observed power spectrum therefore gives the angular and redshift intervals corresponding to the sonic horizon. The peaks in the angular spectrum are proportional to $d_T(z)/a_s$ and those in the redshift spectrum to $d_H(z)/a_s$. $a_s \sim 105h^{-1}Mpc$ is the acoustic horizon comoving size at recombination, $d_T(z) = (1+z)d_A$ is the comoving angular distance and $d_H = c/H(z)$ is the Hubble distance (see Eq. 6):

$$d_H = \frac{c}{H(z)} = \frac{c/H_0}{\sqrt{\Omega_\Lambda + \Omega_m(1+z)^3}} \quad d_T = \int_0^z d_H(z)dz \quad (40)$$

z		0.5	1.0	1.5	2.0	2.5
No Noise	$\sigma(k_{BAO\perp})/k_{BAO\perp} (\%)$	1.8	0.8	0.6	0.5	0.5
	$\sigma(k_{BAO\parallel})/k_{BAO\parallel} (\%)$	3.0	1.3	0.9	0.8	0.8
Noise without Transfer Function (3-months/redshift)	$\sigma(k_{BAO\perp})/k_{BAO\perp} (\%)$	2.3	1.8	2.2	2.4	2.8
	$\sigma(k_{BAO\parallel})/k_{BAO\parallel} (\%)$	4.1	3.1	3.6	4.3	4.4
Noise with Transfer Function (3-months/redshift)	$\sigma(k_{BAO\perp})/k_{BAO\perp} (\%)$	3.0	2.5	3.5	5.2	6.5
	$\sigma(k_{BAO\parallel})/k_{BAO\parallel} (\%)$	4.8	4.0	6.2	9.3	10.3
Optimized survey (Observation time : 3 years)	$\sigma(k_{BAO\perp})/k_{BAO\perp} (\%)$	3.0	2.5	2.3	2.0	2.7
	$\sigma(k_{BAO\parallel})/k_{BAO\parallel} (\%)$	4.8	4.0	4.1	3.6	4.3

Table 7. Sensitivity on the measurement of $k_{BAO\perp}$ and $k_{BAO\parallel}$ as a function of the redshift z for various simulation configuration. 1st row: simulations without noise with pure cosmic variance; 2nd row: simulations with electronics noise for a telescope with dishes; 3th row: simulations with same electronics noise and with correction with the transfer function ; 4th row: optimized survey with a total observation time of 3 years (3 months, 3 months, 6 months, 1 year and 1 year respectively for redshift 0.5, 1.0, 1.5, 2.0 and 2.5).

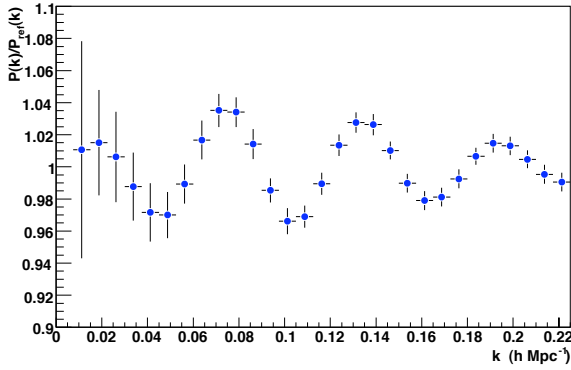


Fig. 16. 1D projection of the power spectrum averaged over 100 simulations of the packed cylinder array b . The simulations are performed for the following conditions: a system temperature, $T_{sys} = 50K$, an observation time, $T_{obs} = 1$ year, a solid angle of $1\pi sr$, an average redshift, $z = 1.5$ and a redshift depth, $\Delta z = 0.5$. The H_I power spectrum is divided by an envelop curve $P(k)_{ref}$ corresponding to the power spectrum without baryonic oscillations and the background estimated by a fit is subtracted. The errors are the RMS of the 100 distributions for each k bin and the dots are the mean of the distribution for each k bin.

The quantities d_T , d_H and a_s all depend on the cosmological parameters. Figure 17 gives the angular and redshift intervals as a function of redshift for four cosmological models. The error bars on the lines for $(\Omega_M, \Omega_\Lambda) = (0.27, 0.73)$ correspond to the expected errors on the peak positions taken from Table 7 for the four-month runs with the packed array. We see that with these uncertainties, the data would be able to measure w at better than the 10% level.

To estimate the sensitivity to parameters describing dark energy equation of state, we follow the procedure explained in (Blake and Glazebrook (2003)). We can introduce the equation of state of dark energy, $w(z) = w_0 + w_a \cdot z/(1+z)$ by replacing Ω_Λ in the definition of $d_T(z)$ and $d_H(z)$, (Eq. 40) by:

$$\Omega_\Lambda \rightarrow \Omega_\Lambda \exp \left[3 \int_0^z \frac{1 + w(z')}{1 + z'} dz' \right] \quad (41)$$

where Ω_Λ^0 is the present-day dark energy fraction with respect to the critical density. Using the relative errors on $k_{BAO\perp}$ and $k_{BAO\parallel}$ given in Tab. 7, we can compute the Fisher matrix for five cosmological parameter: $(\Omega_m, \Omega_b, h, w_0, w_a)$. Then, the combination

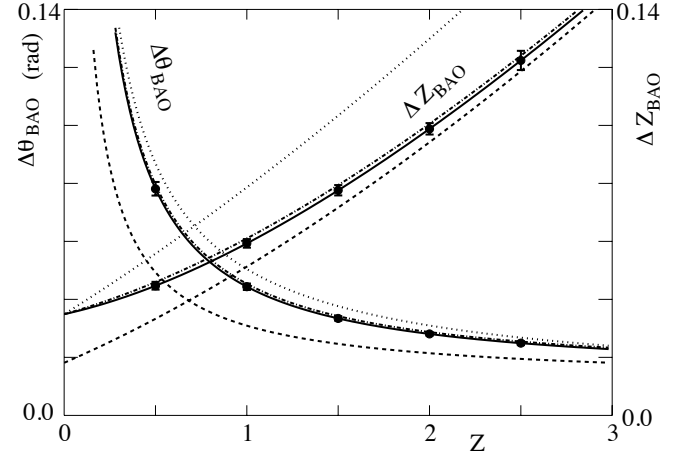


Fig. 17. The two “Hubble diagrams” for BAO experiments. The four falling curves give the angular size of the acoustic horizon (left scale) and the four rising curves give the redshift interval of the acoustic horizon (right scale). The solid lines are for $(\Omega_M, \Omega_\Lambda, w) = (0.27, 0.73, -1)$, the dashed for $(1, 0, -1)$ the dotted for $(0.27, 0, -1)$, and the dash-dotted for $(0.27, 0.73, -0.9)$. The error bars on the solid curve correspond to the four-month run (packed array) of Table 7.

of this BAO Fisher matrix with the Fisher matrix obtained for Planck mission, allows us to compute the errors on dark energy parameters. The Planck Fisher matrix is obtained for the 8 parameters (assuming a flat universe): $\Omega_m, \Omega_b, h, w_0, w_a, \sigma_8, n_s$ (spectral index of the primordial power spectrum) and τ (optical depth to the last-scatter surface).

For an optimized project over a redshift range, $0.25 < z < 2.75$, with a total observation time of 3 years, the packed 400-dish interferometer array has a precision of 12% on w_0 and 48% on w_a . The Figure of Merit, the inverse of the area in the 95% confidence level contours is 38. Finally, Fig. 18 shows a comparison of different BAO projects, with a set of priors on (Ω_m, Ω_b, h) corresponding to the expected precision on these parameters in early 2010’s. This BAO project based on H_I intensity mapping is clearly competitive with the current generation of optical surveys such as SDSS-III (SDSS-III(2008)).

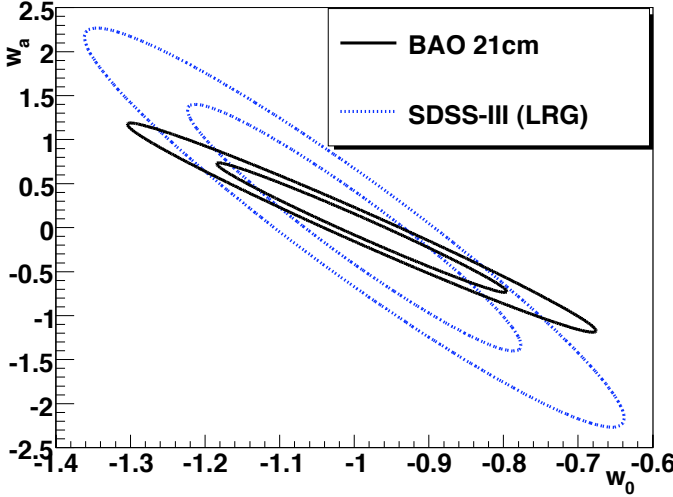


Fig. 18. 1σ and 2σ confidence level contours in the parameter plane (w_0, w_a) for two BAO projects: SDSS-III (LRG) project (blue dotted line), 21 cm project with HI intensity mapping (black solid line).

6. Conclusions

The 3D mapping of redshifted 21 cm emission through *Intensity Mapping* is a novel and complementary approach to optical surveys to study the statistical properties of the large scale structures in the universe up to redshifts $z \lesssim 3$. A radio instrument with large instantaneous field of view ($10\text{--}100\text{ deg}^2$) and large bandwidth ($\gtrsim 100\text{ MHz}$) with ~ 10 arcmin resolution is needed to perform a cosmological neutral hydrogen survey over a significant fraction of the sky. We have shown that a nearly packed interferometer array with few hundred receiver elements spread over an hectare or a hundred beam focal plane array with a ~ 100 meter primary reflector will have the required sensitivity to measure the 21 cm power spectrum. A method to compute the instrument response for interferometers has been developed and we have computed the noise power spectrum for various telescope configurations. The Galactic synchrotron and radio sources are a thousand time brighter than the redshifted 21 cm signal, making the measurement of this latter signal a major scientific and technical challenge. We have also studied the performance of a simple foreground subtraction method through realistic models of the sky emissions in the GHz domain and simulation of interferometric observations. We have been able to show that the cosmological 21 cm signal from the LSS should be observable, but requires a very good knowledge of the instrument response. Our method has allowed us to define and compute the overall *transfer function* or *response function* for the measurement of the 21 cm power spectrum. Finally, we have used the computed noise power spectrum and $P(k)$ measurement response function to estimate the precision on the determination of Dark Energy parameters, for a 21 cm BAO survey. Such a radio survey could be carried using the current technology and would be competitive with the ongoing or planned optical surveys for dark energy, with a fraction of their cost.

References

Abdalla, F.B. & Rawlings, S. 2005, MNRAS, 360, 27

- Albrecht, A., Bernstein, G., Cahn, R. *et al.* (Dark Energy Task Force) 2006, arXiv:astro-ph/0609591
- Ansari R., J.-M. Le Goff, C. Magneville, M. Moniez, N. Palanque-Delabrouille, J. Rich, V. Ruhlmann-Kleider, & C. Yèche, 2008, arXiv:0807.3614
- Barkana, R., and Loeb, A. 2007, Rep. Prog. Phys, 70, 627
- Blake, C. & Glazebrook, K. 2003, ApJ, 594, 665
- Glazebrook, K. & Blake, C. 2005 ApJ, 631, 1
- Blake, Davis, T., Poole, G.B. *et al.* 2011, MNRAS, (accepted, arXiv:1105.2862)
- Binney J. & Merrifield M., 1998 *Galactic Astronomy* Princeton University Press
- Bowman, J. D., Barnes, D.G., Briggs, F.H. *et al.* 2007, AJ, 133, 1505-1518
- Bowman, J. D., Morales, M., Hewitt, J.N., 2009, ApJ, 695, 183-199
- Chang, T., Pen, U.-L., Peterson, J.B. & McDonald, P. 2008, Phys. Rev. Lett., 100, 091303
- Cole, S. Percival, W.J., Peacock, J.A. *et al.* (the 2dFGRS Team) 2005, MNRAS, 362, 505
- Condon J. J., Cotton W. D., Greisen E. W., Yin Q. F., Perley R. A., Taylor, G. B., & Broderick, J. J. 1998, AJ, 115, 1693
- Eisenstein D. & Hu W. 1998, ApJ 496:605-614 (astro-ph/9709112)
- Eisenstein D. J., Zehavi, I., Hogg, D.W. *et al.*, (the SDSS Collaboration) 2005, ApJ, 633, 560
- Eisenstein D. J., Weinberg, D.H., Agol, E. *et al.*, 2011, arXiv:1101.1529
- Furlanetto, S., Peng Oh, S. & Briggs, F. 2006, Phys. Rep., 433, 181-301
- Haslam C. G. T., Salter C. J., Stoffel H., Wilson W. E., 1982, Astron. & Astrophys. Supp. Vol 47, (<http://lambda.gsfc.nasa.gov/product/foreground/>)
- Jackson, C.A. 2004, New A, 48, 1187
- Philip Lah, Michael B. Pracy, Jayaram N. Chengalur *et al.* 2009, MNRAS, 399, 1447
- Lang, K.R. *Astrophysical Formulae*, Springer, 3rd Edition 1999
- Larson, D., *et al.* (WMAP) 2011, ApJS, 192, 16
- LSST Science book, LSST Science Collaborations, 2009, arXiv:0912.0201
- Madau, P., Meiksin, A. and Rees, M.J., 1997, ApJ475, 429
- McDonald P., Seljak, U. and Burles, S. *et al.* 2006, ApJS, 163, 80
- McDonald P., Eisenstein, D.J. 2007, Phys Rev D 76, 6, 063009
- Mauskopf, P. D., Ade, P. A. R., de Bernardis, P. *et al.* 2000, ApJ, 536, 59
- Morales, M., Bowman, J.D., Hewitt, J.N., 2006, ApJ, 648, 767-773
- de Oliveira-Costa, A., Tegmark, M., Gaensler, B. M. *et al.* 2008, MNRAS, 388, 247-260
- Peterson, J.B., Bandura, K., & Pen, U.-L. 2006, arXiv:0606104
- Percival, W.J., Nichol, R.C., Eisenstein, D.J. *et al.*, (the SDSS Collaboration) 2007, ApJ, 657, 645
- Percival, W.J., Reid, B.A., Eisenstein, D.J. *et al.*, 2010, MNRAS, 401, 2148-2168
- Rottgering H.J.A., Braun, r., Barthel, P.D. *et al.* 2006, arXiv:astro-ph/0610596
- SDSS-III 2008, <http://www.sdss3.org/collaboration/description.pdf>
- Science with the Square Kilometre Array*, eds: C. Carilli, S. Rawlings, New Astronomy Reviews, Vol.48, Elsevier, December 2004
- <http://www.skatelescope.org/pages/page.sciencegen.htm>
- Seo, H.J. Dodelson, S., Marriner, J. *et al.* 2010, ApJ, 721, 164-173
- Tegmark, M. & Zaldarriaga, M., 2009, Phys. Rev. D, 79, 8, p. 083530
- Thompson, A.R., Moran, J.M., Swenson, G.W. *Interferometry and Synthesis in Radio Astronomy*, John Wiley & sons, 2nd Edition 2001
- Wolfe, A. M., Gawiser, E. & Prochaska, J.X. 2005 ARA&A, 43, 861
- Wyithe, S., Loeb, A. & Geil, P. 2008, MNRAS, 383, 1195
- Zwaan, M.A., Meyer, M.J., Staveley-Smith, L., Webster, R.L. 2005, MNRAS, 359, L30